5-2017

Feasibility of Using Oxide Thickness Measurements for Predicting Crack Growth Rates in P91 Steel Components

Ralph Edward Huneycutt IV
University of Arkansas, Fayetteville

Feasibility of Using Oxide Thickness Measurements for Predicting Crack Growth Rates in P91 Steel Components

A thesis submitted in partial fulfillment
of the requirements for the degree of
Master of Science in Mechanical Engineering

by

Ralph E. Huneycutt IV
University of Arkansas
Bachelor of Science in Mechanical Engineering, 2014

May 2017
University of Arkansas

This thesis is approved for recommendation to the Graduate Council.

Dr. Ashok Saxena
Thesis Director

Dr. Rick J. Couvillion
Committee Member

Dr. Paul C. Millett
Committee Member

Abstract

There are only few methods available for predicting the age of cracks that are found in high temperature structural components during service; among the promising ones is the oxide thickness measurement technique. Oxide thickness profiles are taken from crack surfaces of components and used for predicting the rates of crack propagation. This technique is particularly suitable for high temperature components fabricated from ferritic steels commonly used in power plants that run on fossil fuels. To implement this technique, it is necessary to fully understand the kinetics of high temperature oxidation in these steels. In this study, the oxidation characteristics of an American Society of Testing and Materials (ASTM) Grade P91 ferritic steel used in high temperature piping is characterized.

The literature shows that there are four primary mechanisms that influence the oxide thickness during high temperature exposure. Initially, the oxide thickness increases in a linear fashion with time and then as steady-state conditions are established, the parabolic relationship takes over. Multiple types of oxides with different rate characteristics can also form. Oxide degradation can occur by spallation due to porosity and formation of cracks. Evaporation or volatility can also occur and result in loss of oxide thickness. These factors must be considered in oxide thickness analysis to determine crack growth history.

Two sets of laboratory experiments were conducted. The first consisted of measurement of oxide thicknesses after exposure to high temperature for various periods to determine the oxidation kinetics. The oxidized samples were subjected to SEM examination and measurements of physical properties such as density and porosity levels. The second set of experiments consisted

of measuring the oxide layer thickness on the fracture surfaces of creep-fatigue crack growth samples tested as part of a previous study where the crack growth rates were measured. These reported measurements are used to compare with the predicted crack growth rates from the analytical models that are developed as part of this study. The success of the technique is measured by finding the correlation coefficient, which is within a factor of 2.58.

Acknowledgements

I would like to thank my thesis advisor Dr. Ashok Saxena, Distinguished Professor and Dean Emeritus, of the Mechanical Engineering Department at the University of Arkansas. He constantly was able to steer me into the right direction, while not micromanaging me. Without his insights and support this work would not have been possible.

I would also like to thank Dr. Kee Bong Yoon in the School of Mechanical Engineering at Chung-Ang University in South Korea. I am grateful for his advisement during our meeting and support during this project.

Finally, I would like to express my gratitude to my family and especially my wife for providing me with support and encouragement during my studies, research, and writing of this thesis. This accomplishment would not have been possible without them. Thank you.

Table of Contents

List of Tables

List of Figures

I. Introduction and Research Objectives

The ability to operate fossil-fuel-fired power plants reliably and to boost their operating temperature capability to attain higher energy conversion efficiencies is essential for the future of the electric power generation industry. Several components of power plants such as reheat piping, heat recovery steam generator (HRSG) Boilers, turbine casings, steam headers and turbine rotors are subjected to high temperatures and periodic cyclic loading during their operation that cause damage in the form of creep cavities and the formation of cracks due to the phenomena such as creep and creep-fatigue interactions. The operators of such equipment frequently use plastic replicas to monitor the progression of damage. Accurate models are needed to assess the level of damage and the remaining life to make run/repair/retire decisions.

In the past twenty years, considerable progress has been made in the ability to predict crack growth and damage propagation under the conditions of creep and creep-fatigue [1-6]. Due to the large number of variables and material constants needed in the analysis, the variability in the life predictions can be as high as a factor of ten [7]. The use of oxide thickness measurements from the extracted damaged regions of the reheat steam pipes to directly measure crack growth rates during service to verify predictions from the analytical crack growth models is explored in this study. The comparisons between theoretical predictions and actual measurements can be to improve the accuracy of the analytical models [7].

The material chosen for this research is ASTM Grade P91 steel used in steam pipes in advanced power plants. The test material is taken from an ex-service steam pipe but rejuvenated to recover the original microstructure. This material has been used as the test material for conducting two round–robins to verify test standards developed by American Society for Testing and Materials

(ASTM) in the areas of creep-fatigue crack formation and crack growth, E-2714-09 and E-2760-10, respectively [8,9]. Consequently, considerable crack growth data and tested specimen fracture surfaces were available to support the project objectives.

II. Objective

Figure 1 shows a snapshot of an idealized crack growing in a pipe during service with the elevated temperatures and corrosive environment causing oxide growth to occur.

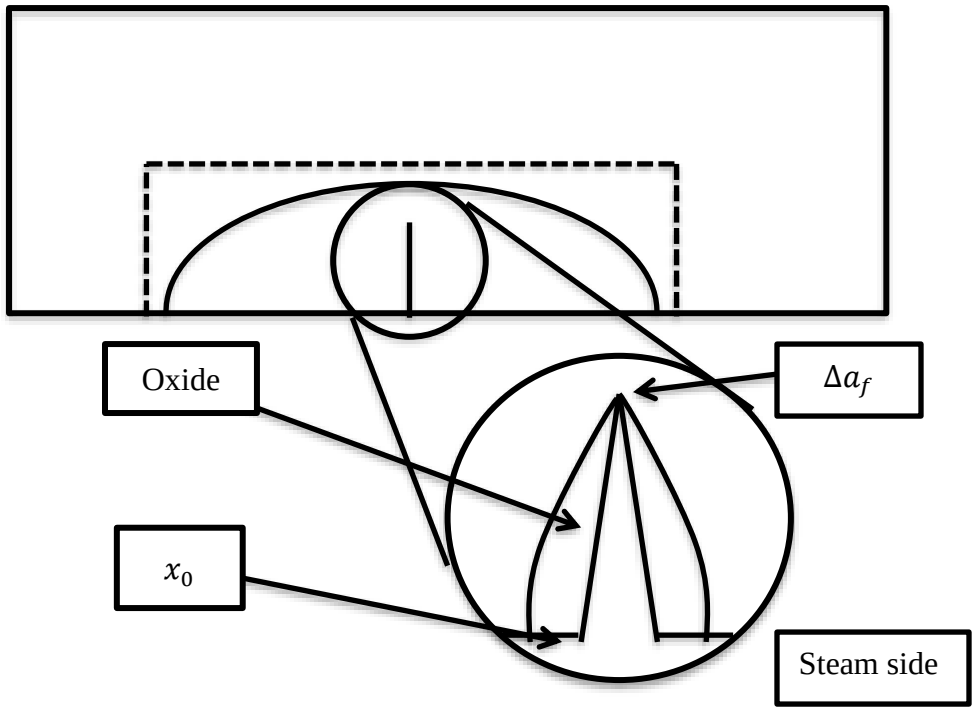

Figure 1 – Schematic of Pipe in Service with Crack with Oxide Growth on the Crack Surface

The purpose of this research is to explore if oxide thickness growth along the crack surface of P91 steel components at elevated temperatures can be used to predict the crack growth rates. In order to use the oxide thickness to predict crack growth rates the following steps need to be made,

- Literature review of the kinetics of the oxide thickness.
- Experimental process to create oxidized samples for characterizing the oxidation kinetics.
- Comparison of measured crack growth rates in laboratory specimens to predicted crack growth rates from oxide thickness measurements.

The literature review begins with a description of the growth kinetics of a simplified model that considers only a single layer of oxide.

III. Literature Review

A. Single Layer Oxidation Kinetics

A.i) The Parabolic Law

The idea of using the oxide thickness as a parameter of predicting the age of a cracks and estimating propagation rates was first introduced by L.W. Pinder [10]. In this paper, the kinetics of oxide growth is used to determine the amount of service time the crack has been in the component and the rate at which it has been growing. A basic model of oxide growth kinetics can be derived through the illustration shown in Figure 2 for a diffusion-controlled oxidation process.

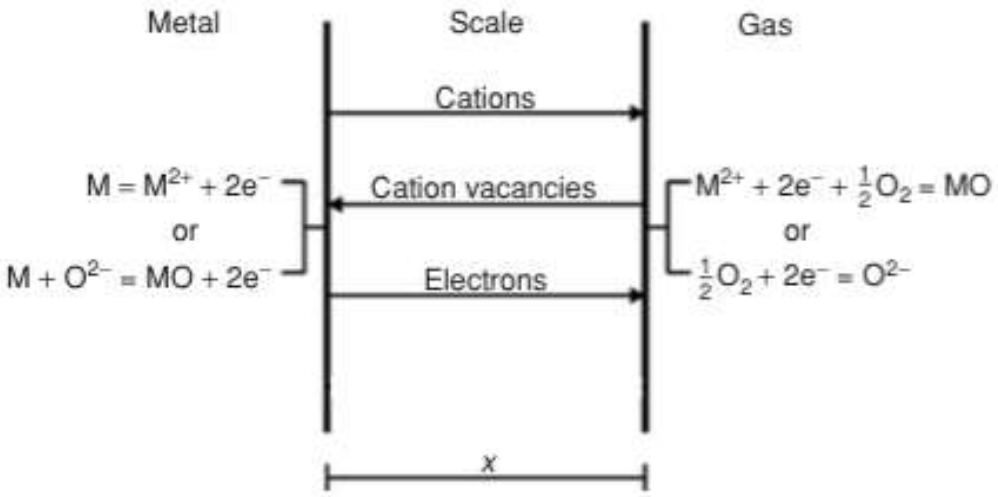

Figure 2 – Diffusion-Controlled Oxidation mechanism [11]

Figure 2 shows the flow of cations or metal ions and electrons between the metal/scale and gas scale interfaces with the balance of cation vacancies, which can be represented as fluxes in the following equation,

$$J_m = -J_V \tag{1}$$

where J_m is the flux of the metal ions and the electrons and J_v is the flux of the cation and electron vacancies. Using Eq. 1, the flux of the metal atoms into the oxide scale can be rewritten into,

$$J_m = D_{v,m} \frac{dC_{v,m}}{dx} \tag{2}$$

where $D_{v,m}$ is the vacancy diffusion coefficient in the metal and $\frac{dC_{v,m}}{dx}$ is the gradient of vacancy concentration in the x-direction. Next, we assume that the scale is thick enough for the metal/scale and scale/gas interfaces to be in thermodynamic equilibrium. This assumption allows the change in concentration in the x-direction to be altered in Eq. 2 into,

$$J_m = D_{v,m} \frac{C''_{v,m} - C'_{v,m}}{x} \tag{3}$$

where $C''_{v,m}$ is the composition at the scale/gas interface, $C'_{v,m}$ is the composition at the metal/scale interface, and x is the length (or thickness) of the scale. The next modeling step is to relate the flux of the metal atoms to the rate of change of the scale thickness using the following relationship,

$$J_m = \frac{1}{V_s} \frac{dx}{dt} \tag{4}$$

Where V_s is the molar volume of the scale and $\frac{dx}{dt}$ is the rate of change in the oxide thickness over time. Combining Eq. 3 and 4 leads to the rate of change of the oxide scale thickness in terms of the vacancy concentration across the oxide scale,

$$\frac{dx}{dt} = V_s D_{v,m} \frac{C''_{v,m} - C'_{v,m}}{x} \tag{5}$$

Using the assumptions that the system is in steady state and under isothermal conditions, the following terms can be combined together in a single term known as the parabolic rate constant, k_p,

$$k_p = V_s D_{v,m}\left(C''_{v,m} - C'_{v,m}\right) \tag{6}$$

Using Eq. 5 and 6 the rate of change of the oxide scale thickness is written as,

$$\frac{dx}{dt} = \frac{k_p}{x} \tag{7}$$

Integrating Eq. 7 from t =0 when x =0 to an arbitrary time, t, corresponding to the oxide thickness, x, yields the following relationship,

$$\int_0^x x\,dx = \int_0^t k_p\,dx$$

$$x^2 = 2k_p t \tag{8}$$

Equation 8 is known as the parabolic rate equation explicitly relating oxide thickness to the time of exposure to the oxidizing environment. The factor of 2 in Equation 8 is incorporated into the parabolic rate constant, k_p, during the data analysis but in Birks, Meier, and Pettit[11] and Young[13] the factor of 2 is kept. Therefore, the oxidation kinetics are represented by the in the following relationship for isothermal conditions,

$$x^2 = k_p t \tag{9}$$

A.ii) Dependence of the Parabolic Rate Constant on Temperature and Pressure

The parabolic rate constant, $k_p$varies with temperature through its relationship with the self-diffusion coefficient that is dependent on the kinetics of vacancy diffusion. The self-diffusion coefficient, D^*, in a three-dimensional crystal is [12],

$$D^* = \frac{\lambda^2 \Gamma_a}{6} \tag{10}$$

where D^* is the self-diffusion coefficient, λ is the mean atomic spacing, and Γ_a is the atomic jump frequency. The vacancy diffusion coefficient in a three-dimensional system is,

$$D_v = \frac{\lambda^2 \Gamma_v}{6} \tag{11}$$

where Γ_v is the vacancy jump frequency. The two jump frequencies are related because the number of atomic jumps equals the number of vacancy jumps; thus,

$$n_v\Gamma_v = n_a\Gamma_a \tag{12}$$

where n_v is the moles of vacancies and n_a is the moles of atoms. Since the total moles of the system, n, is equal to the moles of vacancies plus the mole of atoms, dividing both sides of the equation by the total moles of the system modifies Eq. 12 into,

$$X_v\Gamma_v = X_a\Gamma_a \tag{13}$$

where X_v is the mole fraction of vacancies and X_a is the atomic mole fraction of atoms. Since the $X_a \approx 1$, Eq. 13 can be simplified into,

$$X_v\Gamma_v = \Gamma_a \tag{14}$$

The reason Eq.14 is significant is because the self-diffusion coefficient is also equal to,

$$D^* = D_0 \exp\left(-\frac{Q}{RT}\right) \tag{15}$$

where D_0 is the pre-exponential coefficient, Q is the activation energy, R is the ideal gas constant, and T is the temperature, which means the diffusion coefficient is exponentially dependent on temperature and therefore also k_p as seen in Figure 3 for Ni. The diffusion coefficient is plotted in an Arrhenius type plot for lattice diffusion and also grain boundary diffusion through low angle and high angle grain boundaries. It also plots the diffusion of oxygen in Ni.

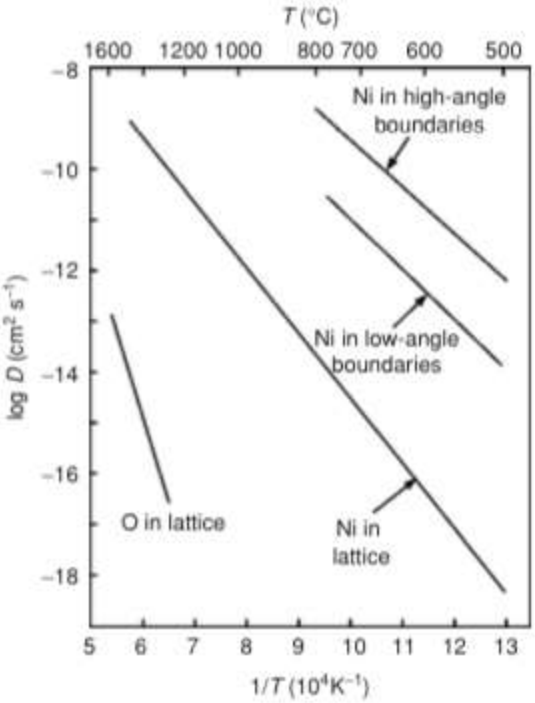

Figure 3 – Graphical Representation of the dependence of the diffusion coefficient of Ni on Temperature [11]

The dependence of the parabolic rate constant on the partial pressure of O_2 is embedded in the relationship between the partial pressure of the corrosive gas and the vacancy concentration [11],

$$C_v = const * (p_{gas})^{\frac{1}{n}} \tag{16}$$

where p_{gas} is the partial pressure of the corrosive gas and n is a dimensionless number determined by the corrosive and the specific metal. From Eq. 16 the variation of the parabolic rate can be seen,

$$k_p \propto \left[\left(p''_{gas}\right)^{\frac{1}{n}} - \left(p'_{gas}\right)^{\frac{1}{n}} \right] \tag{17}$$

where p''_{gas} is the partial pressure of oxygen at the scale/gas interface and p'_{gas} is the partial pressure of oxygen at the metal/scale interface.

Figure 4 shows the variation of the parabolic rate constant with partial pressure. At a certain value of partial pressure for each temperature, the assumption of one phase oxide scale growth breaks down and there is a sharp discontinuity in the relationship between the parabolic rate constant and the partial pressure of oxygen. This is explained by the presence of two oxide phases and will be explored further in Section 2 of the literature review.

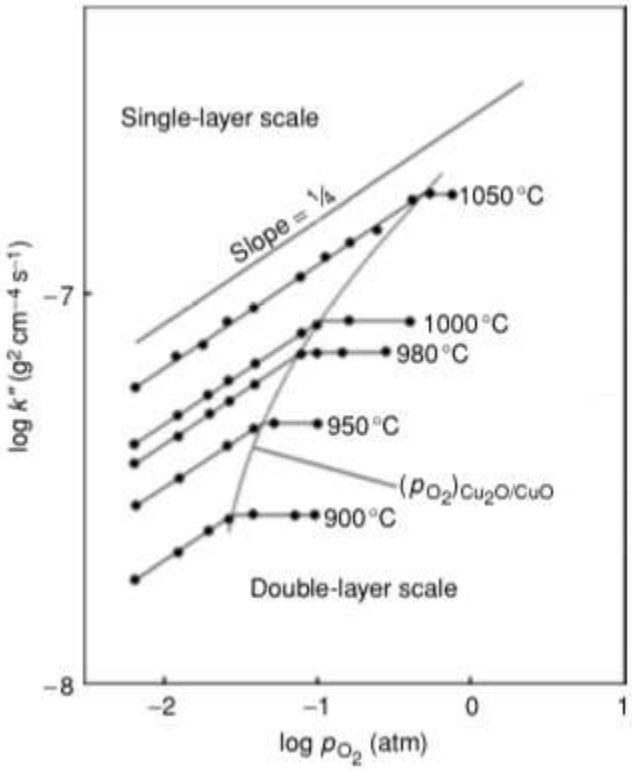

Figure 4 – Variation of parabolic rate constant with oxygen partial pressure and temperature for the oxidation of copper [10]

The next step in understanding the parabolic rate constant comes from its measurement.

A.iii) Measurement of k_p

Values of the parabolic rate constant are normally reported as a weight gain per unit area in units of $mass * area^{-2} * time^{-1}$ such as in Figure 4. The prevalence of this unit convention is because of the ability to use one sample to collect the kinetics profile for a chosen atmosphere [11]. The experimental setup for measuring the weight gain per unit area k_p is shown in Figure 5.

From the weight gain per unit area data, the user can derive a parabolic rate constant using the following equation,

$$\left(\frac{\Delta W}{A}\right)^2 = k_p t \tag{18}$$

where ΔW is the change in weight and A is the exposed area of the sample where oxidation occurs. The following equation can be used to determine oxide thickness for single phase scale growth [13],

$$X = \frac{1}{16\rho_s}\frac{\Delta W}{A} \tag{19}$$

where X is the oxide thickness and ρ_s is the density of the scale.

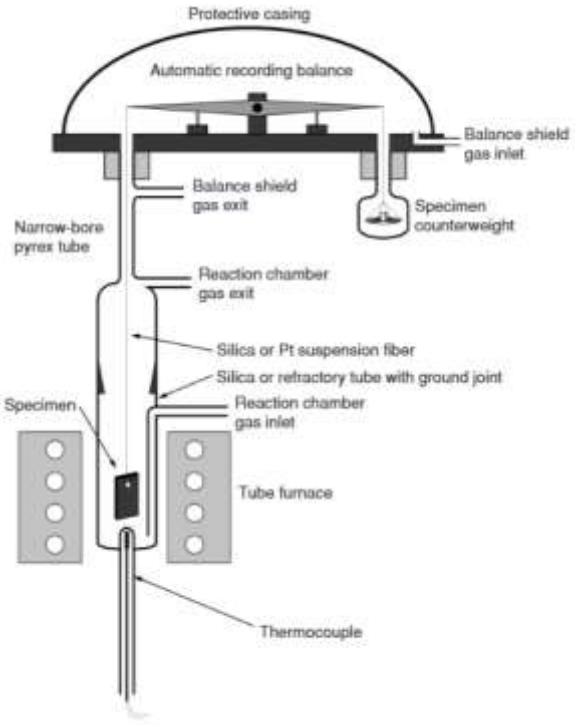

Figure 5 – Typical Experimental Arrangement for Measuring Oxidation Kinetics [11]

The oxide growth on metal may not be a single phase but multiple phases. Multiphase oxide growth can occur depending on the temperature, pressure, and/or thermodynamic processes of oxidation of previously oxidized metals.

B. Two Layer Scale Growth Kinetics

As time progresses under the aforementioned conditions the metal, scales, and gas can have characteristics as schematically shown in Figure 6. The modeling of a two-layer scale growth system, where steady-state conditions are assumed, means that the parabolic scale growth for each of the two layers can be modeled with the follow equation,

$$X_i^{\,2} = k_i t \tag{20}$$

where i =1 for the inner most oxide layer and i = 2 for the outer most oxide layer. Thus, X_i is the scale thickness of the ith layer and k_i is the parabolic rate constant for the same layer. However, it should be noted that $k_i \neq k_p$ for the two layers by themselves. The following equation was derived for a dual-phase oxide with the overall parabolic growth constant, k_{ov}, for the total scale thickness growth [13],

$$k_{ov} = \left(k_1^{\,0.5} + k_2^{\,0.5}\right)^2 \tag{21}$$

From the weight gain method, the "parabolic" rates for each of the scale types can be determined for this system if data is obtained for each scale type. Figure 7 shows an actual two layer scale growth of 1Cr-0.5Mo steel in laboratory air for 1000 hrs at 500 ^{0}C. The picture clearly shows two types of oxides, Fe_2O_3, and Fe_3O_4.

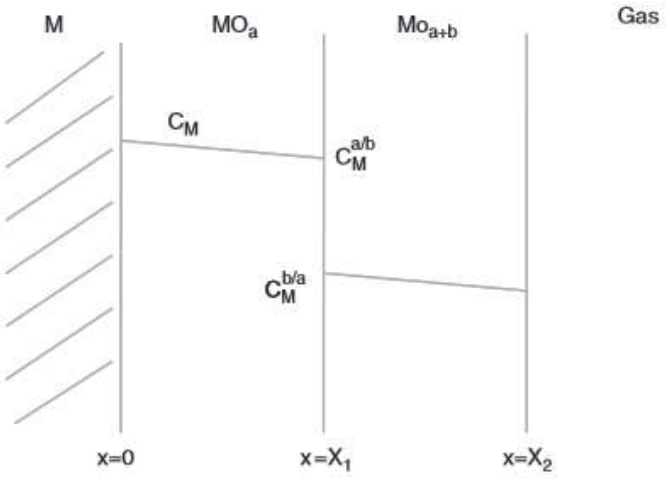

Figure 6 – Schematic View of Two-Layer Scale Growth [13]

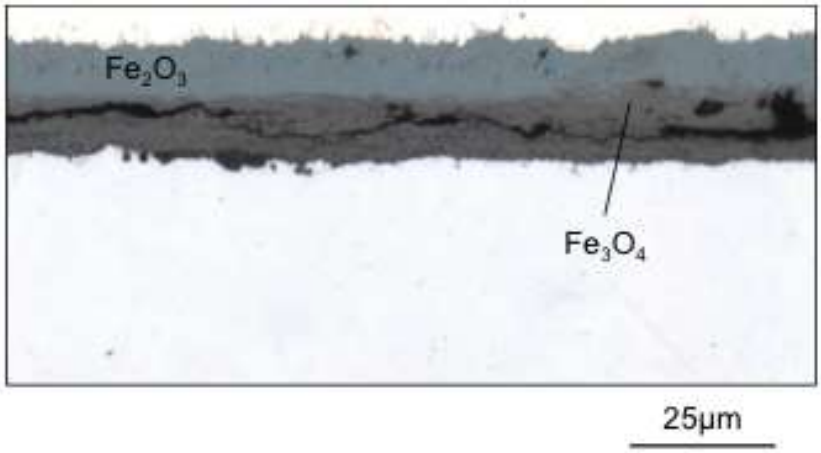

Figure 7 – 1Cr-0.5Mo steel Oxidized in Laboratory air for 1000h at 500^0 C [14]

C. Other Mechanisms Influencing Oxide Thickness

A number of factors of practical significance cause the oxide thickness to deviate from the parabolic law. These include (a) evaporation or volatility of the oxide, (b) spallation of oxide, (c) initial transient behavior of oxidation kinetics at the metal-oxide and oxide-gas interface, and (d) low temperature oxidation that does not follow the parabolic law.

A simple and quick way of checking whether an oxide growing at a given temperature and oxygen partial pressure is liable to volatilize is by use of Ellingham-Richardson Diagram shown in Figure 8.

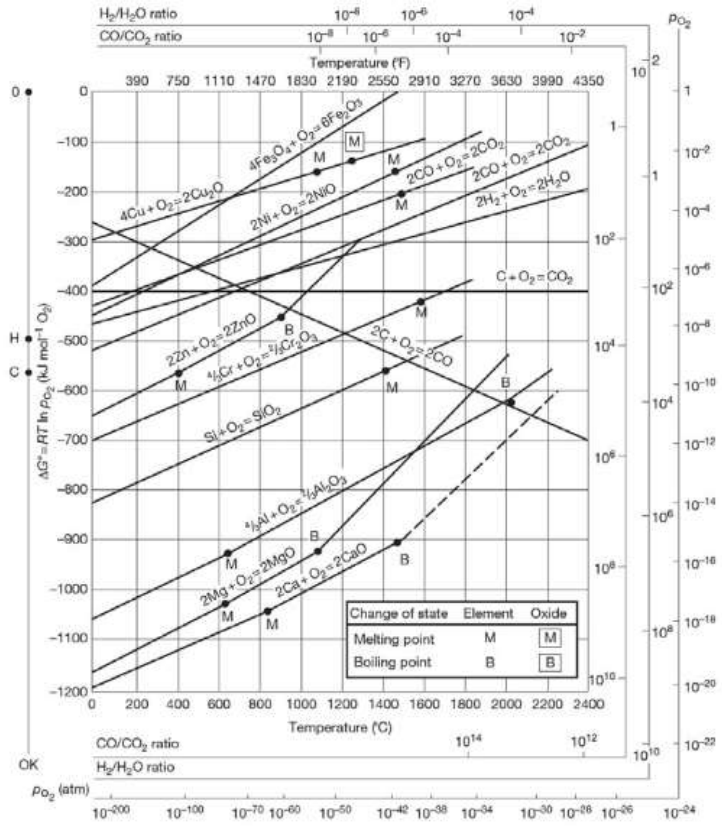

Figure 8 – Ellingham-Richardson Diagram for Selected Oxides [14]

From Figure 8 the standard Gibbs free energies of formations of the shown oxides can be found with,

$$\Delta G_0 = \Delta H_0 - \Delta S_0 T \tag{22}$$

where the linearity of the plot shows that both ΔH_0 and ΔS_0 are approximately constant over the solid until boiling occurs.

Figure 8 can be used to determine the partial pressure of oxygen at which the oxide becomes volatile at a given temperature. If the partial oxygen pressure becomes less than this critical value, the oxide thickness will reduce due to volatility and digress from the parabolic behavior. The procedure for determining the critical partial pressure is outlined as below:

1. Line up a straight edge on the line next to the Gibbs free energy of formation on one of the points dependent on the critical ratio or partial pressure chosen.
    a. If oxygen is the main corrosive agent in the system, place the straight edge on the point labeled O.
    b. If H_2O is the main corrosive agent in the system, place the straight edge on the point labeled H.
    c. If carbon dioxide is the main corrosive agent system place the straight edge on the point labeled C.
2. Keeping one part of the straight edge on the point for the type of corrosive and then rotate the end until the straight edge goes through the intersection of the temperature and the oxide of interest.
3. Follow the line created by the straight edge and read the partial pressure off of the axis of the type of corrosive of interest.

The partial pressure value that is found via this method is known as the equilibrium partial pressure. If the partial pressure of the corrosive is below the equilibrium partial pressure, then the oxide will become volatile and therefore will most likely cause the oxide thickness to reduce. Thus, the oxide thickness will have a negative growth rate after a period of time, which means that the parabolic growth kinetics will break down.

In the above analysis, the scale has been assumed to be sufficiently compact that spallation has not been considered. Oxides have porosities in the scale that can cause cracks due to stresses. As the oxide grows the kinetics will follow a parabolic growth rate with sudden drops in the

thickness as spallation of the oxide scale occurs. This must be accounted for during the use of oxide thickness to determine crack growth rates.

Another deviation from the parabolic kinetics comes from the initial oxidation of the metal and gas interface when thermal equilibrium at the interfaces has not been established. The kinetic path for this is linear until the oxide thickness becomes thick enough to provide enough protective behavior to limit the flux of the metal atoms to the scale/gas interface for oxidation reaction to occur. Until this point the oxide layer is labeled as non-protective, leading to linear kinetics.

Yet another mechanism by which the oxidation kinetics does not follow the parabolic kinetics is if oxidation occurs at low temperatures. At these lower values of approximately 400^0C and lower for most steels [11], the kinetics follow a logarithmic or inverse logarithmic behavior.

Figure 9 schematically shows the weight gain/loss due to the four oxidation mechanisms discussed above. It is highly important to understand the applicable mechanism of oxide formation to correctly interpret the oxide thickness data from service cracks. This will require an extensive experimental program under controlled laboratory conditions as discussed in the next section.

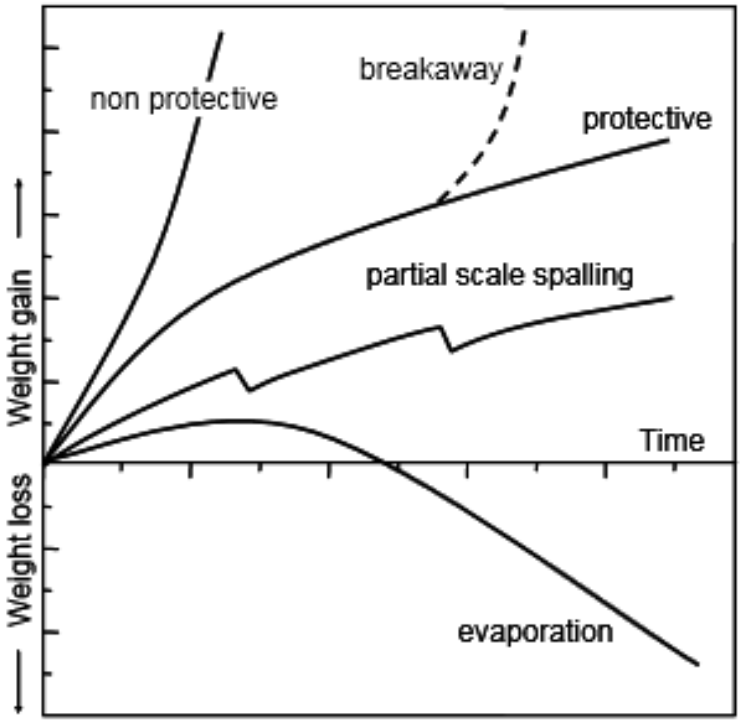

Figure 9 – Different oxidation kinetics frequently encountered in real metal and alloys systems [14].

D. Validity of parabolic oxide kinetics

The actual behavior of oxidation can be seen in Figure 10 and 11 below [15]. In it the parabolic growth predicted by equation 9 is validated, but the initial linearity of the kinetics due to insufficient scale growth is also seen in Figure 11. However, this linearity transitions into steady-state behavior described earlier. The materials used in these experiments are P91, P92, and other steels, which are of substantial interest in the power industry and are continually being researched in various atmospheres to obtain the oxidation behavior. Table 1 shows the parabolic rate constants in air obtained from their data at different temperatures for air.

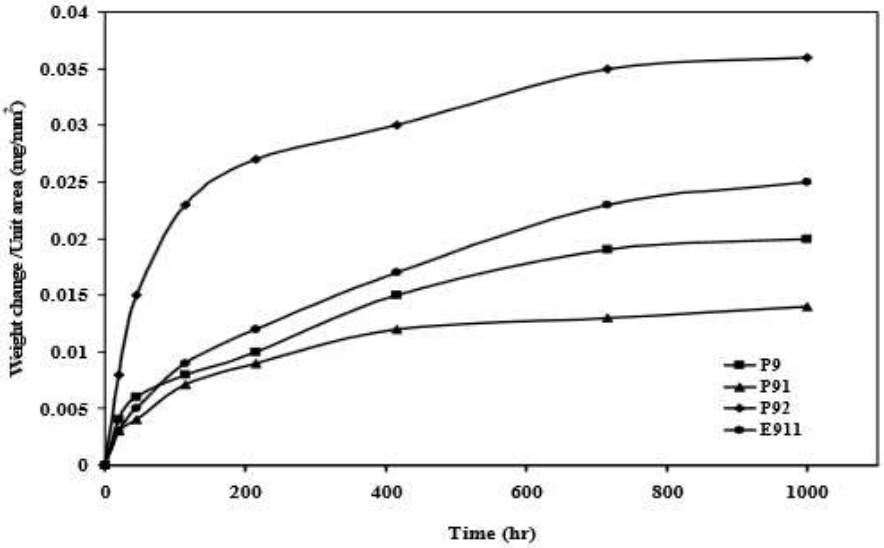

Figure 10 – Weight change vs. Time for oxidation of various ferritic alloys at 873 K in air [15]

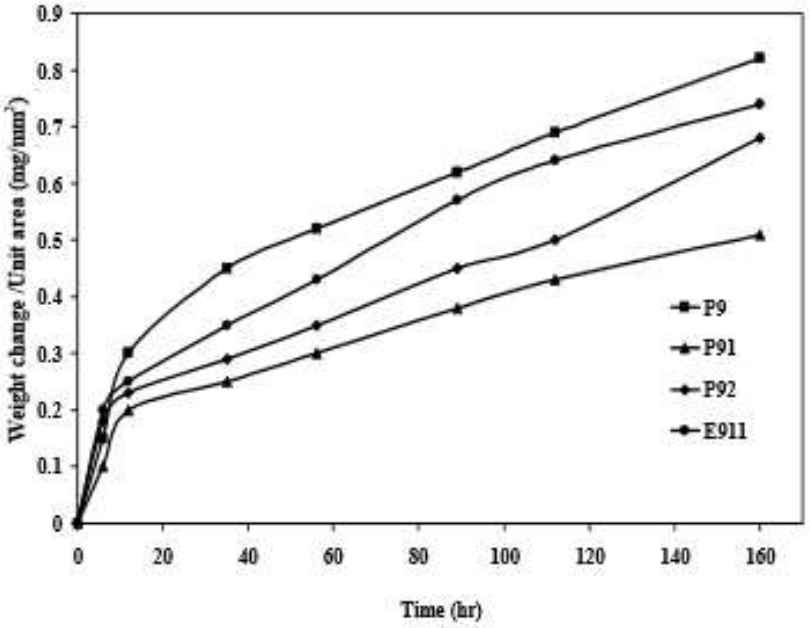

Figure 11 – Weight change vs. Time plots for the same alloys as in Figure 10 at 1073 K in O_2 + 50 % H_2O [15]

Table 1 – Parabolic rate constants in air ($mg^2mm^{-4}hr^{-1}$) [15]

Temperature (K)	P91	P92
873	2E-7	1E-6
973	5E-5	6E-5
1073	0.5E-3	0.8E-3

E. Using Oxide Growth Kinetics to Determine Crack Growth Rates

As was initially mentioned in this literature review, one of the first documentations to use oxide thickness as a parameter to determine age and rates of crack growth in service was by Pinder [10]. In his research, Pinder was able to use equation 9 to transform a graph of the oxide thickness as a function of crack length, shown in Figure 12, into crack length as a function of time, shown in Figure 13, from which the crack growth rate at a given time can be found by taking the derivative of the crack length with time.

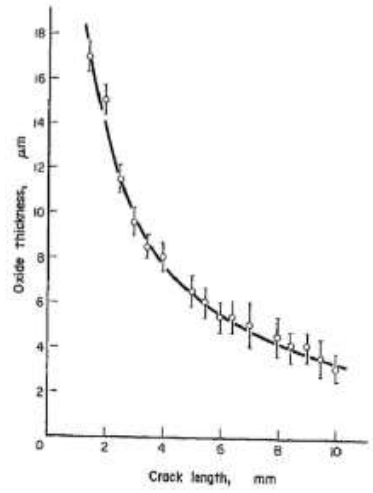

Figure 12– Oxide thickness as a function of crack length for thumbnail defect in C-Mn Steel pipe. [10]

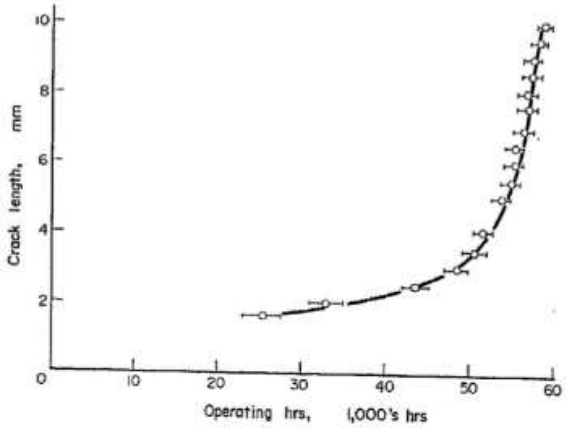

Figure 13 – Crack length as a function of time derived from oxide thickness measurements shown in Figure 12 [10]

The first step in outlining the experiment process of finding if oxide thickness kinetics on crack surfaces can be used to predict crack growth rates was to choose a material. For this study, P91 steel was chosen from a previously conducted study on creep-fatigue crack growth rates as the test material because of the accessibility to crack length versus time data. Also, P91 steel chosen is in extensive use in high temperature components making the study highly technologically relevant.

IV. Experimental Setup and Process

The experimental setup and process can be divided into seven sub-steps as follows:

1. Experimental Setup
    i. Test Material Selection
    ii. Specimen Design and Machining
2. Experimental Process
    i. Sample Preparation
    ii. Pre-Oxidation Weighing
    iii. Oxidation of the Samples in Furnace
    iv. Post-Oxidation Weighing
    v. Application of Protective Ni Coating
    vi. Measurement of Oxide Thickness

This methodology was chosen in accordance with the study by Mathiazhagan and Khanna[15] who also presented results on the same class of materials (ASTM Grade P91).

A. Experimental Setup

A.i) Test Material Chosen for Experiments

The test material chosen is a modified 9% chromium (Cr)-1% molybdenum (Mo) steel that is designated by the ASTM as grade P91 steel wherein the prefix P denotes piping application [16]. All the P91 specimens were obtained from a retired pipe donated by the Electric Power Research Institute (EPRI) Charlotte, USA, shown in Figure 14. The pipe material was re-normalized to ensure consistency with the original tempered martensitic/ferritic microstructure of these steels. The physical dimensions of the pipe section were as follows: outer diameter: 482 mm, wall thickness: 47.5 mm and a length of approximately 1 m. The pipe was cut along its length to

obtain approximately 3 equal sections. The 3 cut segments were respectively labeled as sections 1, 2 and 3 and only the cut Sections 2 and 3 were used in round robins (RRs) conducted to verify test standards for creep-fatigue crack initiation and for crack propagation. A comprehensive collection of all the specimen drawings and machining layouts, along with other test matrix details, used for the current RR is provided in a recent EPRI report and publication [17]. The chemical composition of P91 steel used in the RR testing in weight% is given in Table 2.

Figure 14- Picture of the pipe from which the test material for the program was extracted.

Table 2 – Chemical composition of test material (in weight %)[17]

C	Si	Mn	P	S	Ni	Cr	Mo	As	V	Nb	Al	Cu	N	Sb, Sn	Fe
0.11	0.31	0.45	0.011	0.009	0.19	8.22	0.94	0.005	0.21	0.07	0.006	0.16	0.039	0.001	Bal.

Tensile tests, creep deformation, and rupture tests on P91 steel were conducted at 625^0C to fully characterize the material and the results were reported in reference [17].

A.ii) Sample Design and Creation

The samples for oxidation studies were taken from the halves of three tested compact type C(T) specimens shown in Figure 15. These specimens were subjected to creep-fatigue crack growth

testing as part of the round robin program in support of ASTM Standard E2760-10 [9]. Further details of the material and its mechanical properties can be found in reference 17.

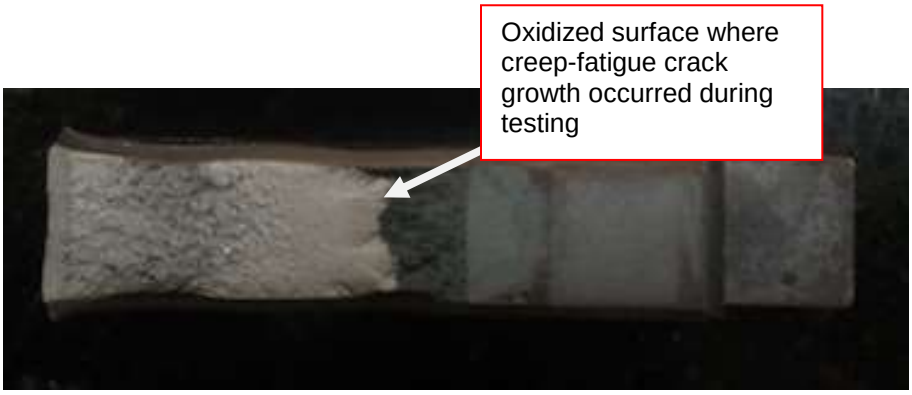

Figure 15 - Picture of a tested creep-fatigue crack growth specimen used for machining the oxidation samples.

Seventeen rectangular oxidation samples (six from each specimen half) with dimensions of 20mm x 10mm x 5mm were machined using the both halves from three tested creep-fatigue crack growth specimens, shown in Figure 16. In-plane sample dimensions were similar to samples used by Mathiazhagan and Khanna but the thickness of our specimens was 5 mm while the other study used a sample thickness of 10 mm. A 3 mm diameter through-hole in the sample was chosen to mount the samples in the furnace.

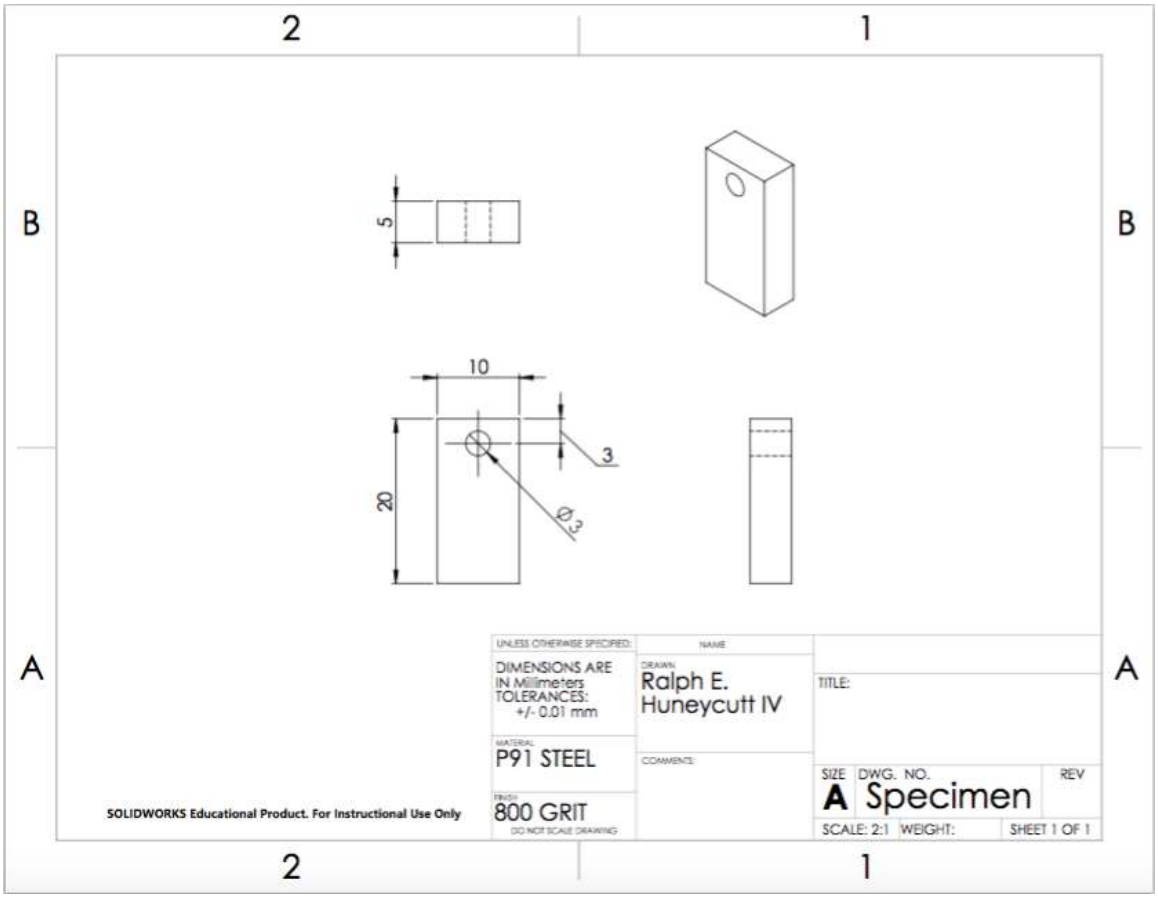

Figure 16 – CAD of Oxidation Samples

B. Experimental Process

B.i) Preparation of Oxidation Samples

The technique for preparation of oxidation samples was similar to the technique used by Mathiazhagan and Khanna [15] with some differences. Mathiazhagan and Khanna's samples were prepared by mechanically polishing up to grit of 800 followed by ultrasonically cleaning with acetone and allowing time to dry before the oxidation test. The end results were data points collected of weight gain of the samples as a function of time of exposure and the test temperature. The polishing process in our experiments consisted of a progression from a coarser to finer grit finishing at a grit number of 800 without an ultrasonic cleaning with acetone. The grit sequence was:

1. *Start with 200 Grit Paper*
2. *Move to 400 Grit paper*
3. *Move to 800 Grit Paper*

The polishing process also included a rotation of 90 degrees [18] between steps in order to have a visual check that the marks left from previous polishing steps from the coarser grit was removed. A special sample holder shown in Figure 17 was fabricated to ensure that the polished surfaces were perpendicular with the normal surfaces. This tool was used to hold the samples while the polishing paper is taped to the work surface as shown in Figure 18. The polishing paper used is the CarbiMet Adhesive Discs with a PSA backing by Buehler.

Figure 17 - A special sample holder created to ensure uniform polish on all surfaces

Figure 18 - Polishing paper taped to the work surface for polishing samples

B.ii) Measurement of Pre-test Sample Mass

Prior to placing the samples in the furnace, the samples were weighed using a Sartorius Cubis MSA225S-100-DI balance shown in Figure 19. The resolution of the balance is 10-micrograms that was considered sufficient for measuring mass gain even in samples with low exposure times. Four separate weight measurements were made and averaged to get an accurate measure of the weight gain.

Figure 19 – Satorius Cubis MSA225S-100-DI used for Measuring Weight Change

B.iii) Oxidation Experiments

Table 3 shows the test matrix for oxidation experiments. Exposure times ranged from 10 hours to 1000 hours and the temperatures from 600 to 650 degrees C.

Table 3 – Test Matrix

Laboratory Air at fixed Temp ^0C	Exposure Time (hr)						
	10	20	50	100	200	500	1000
600	x	x	x	x	x	x	x
625			x	x		x	x
650	x	x	x	x	x	x	

Since there is time lapse between machining samples and testing them in the furnace, machined samples were placed in a desiccator with nitrogen purge to reduce the overall exposure to oxygen

and water vapor in the environment. Additionally, the final polishing and weighing occurred just prior to exposure in the furnace, in those order.

The furnace chosen for oxidizing the samples is the one attached to a 2330 Series Creep/Stress Rupture Testing System, shown in Figure 20 equipped with the ability to digitally control the temperature. Also, this furnace was chosen since this machine is the same/similar used on the C(T) samples, the oxidation samples were made from.

Figure 20 – Picture of the furnace being used for oxidation tests as part of the 2330 Series Creep/Stress Rupture Testing System

A dummy sample of the same material was placed with a thermocouple to monitor the specimen temperature so there would be no need to weld a thermocouple to the actual specimen creating uncertainty during weight measurements as shown in Figure 21.

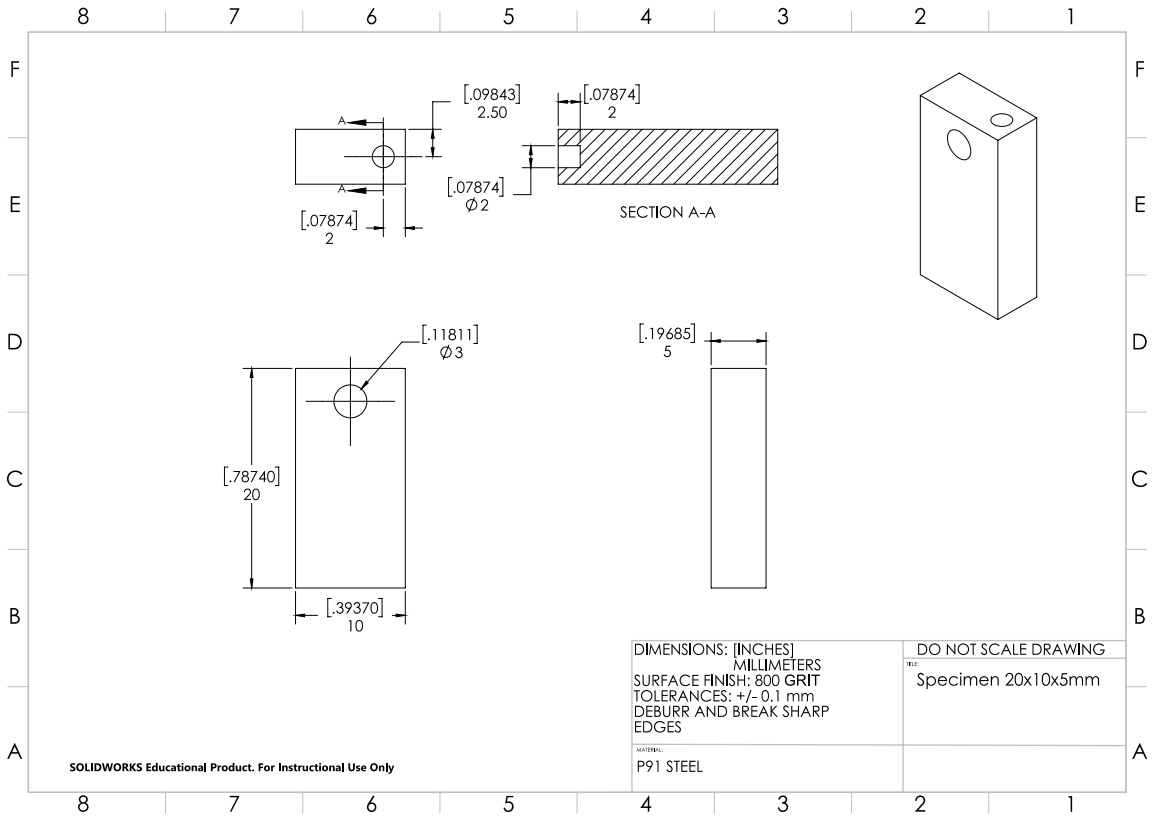

Figure 21 – CAD of Dummy Samples

The stability of the Creep/Stress Rupture Testing System with regard to controlling the furnace temperature was tested using a spare compact specimen. The variation in temperature during the 100 hour run time at 500^0C was less than +/- 0.6 °C as seen in Figure 22.

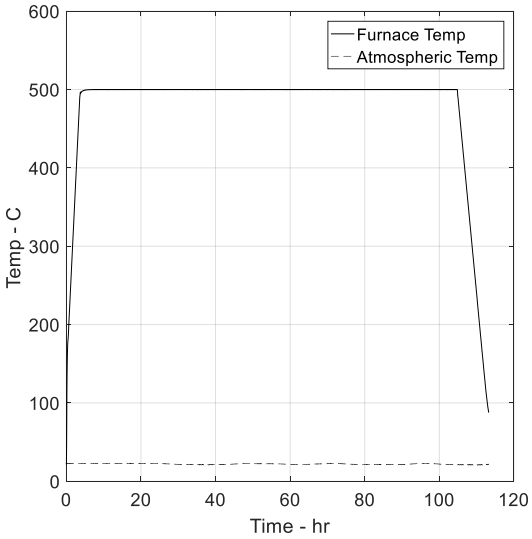

Figure 22– Results from a trial run of the furnace at 500°C for 100 hours

A sample holder was designed as shown in Figure 23. The samples were mounted on the threaded rod, which has the added benefit of making the sample holder support easy to unscrew and remove from the sample. The holes in the top of the sample holders are for the wire to slip through and attach to the frame of the 2330 Series Creep/Stress Rupture Testing System.

Figure 23 – Picture of sample holder from 2 views

B.iv) Post-Test Mass Gain Measurements

The Satorius Cubis MSA225S-100-DI conducted the measurements of the samples post-test weight. As with the pre-test measurements, the samples were weighed four times. The surface nearest to the mounting hole was placed on the scale to minimize damage to the oxide layer characterized in a later step. To determine expected changes in weight, a C(T) specimen was exposed to 500^0C for 100 hours and a mass change of 5.88 mg was measured, confirming that the 10 micro-gram resolution of the weighing balance was sufficient for our purposes.

B.v) Application of Protective Ni Coating

Samples that are Ni coated to protect the oxide from spalling also have the added advantage of providing a good optical contrast for making accurate thickness measurements as shown in Figure 24 [14]. Thus, both fracture surfaces from C(T) specimens and oxidation samples were Ni coated prior to further testing.

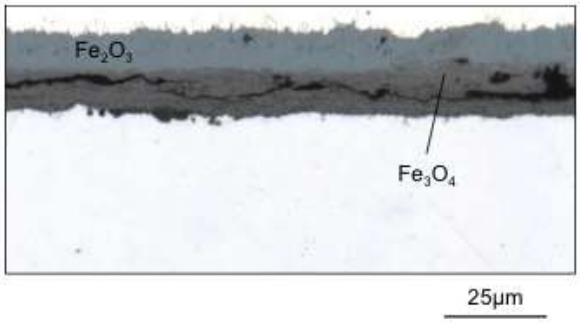

Figure 24 – Optical contrast created by Ni coating oxidized samples [14]

The actual Ni coating of the oxide samples was done using an E-Beam Evaporator, shown in Figure 25 available in the High Density Electronics Center (HiDEC) at the University of Arkansas. The process of applying the Ni coating inside the E-Beam Evaporator chamber involves mounting of the samples to a Si wafer. The samples are fixed to the Si wafer by Kapton tape as shown in Figure 26 for the C(T) specimens. The Ellingham-Richardson diagram [12] was used to ensure that the vacuum levels during e-beam evaporation do not cause the oxide to volatize (or evaporate) due to the vacuum conditions in the E-Beam Evaporator.

Figure 25 – E-Beam Evaporator available for Ni coating samples

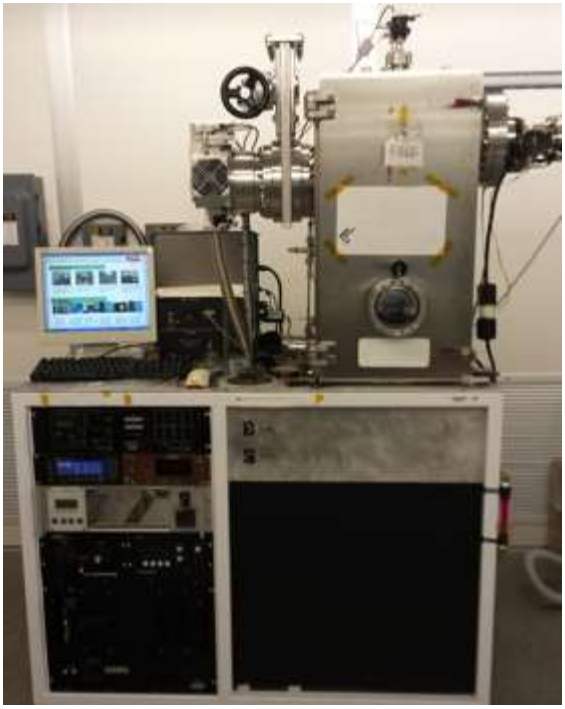

Figure 26 – C(T) samples mounted to Si wafer for application of Ni coating

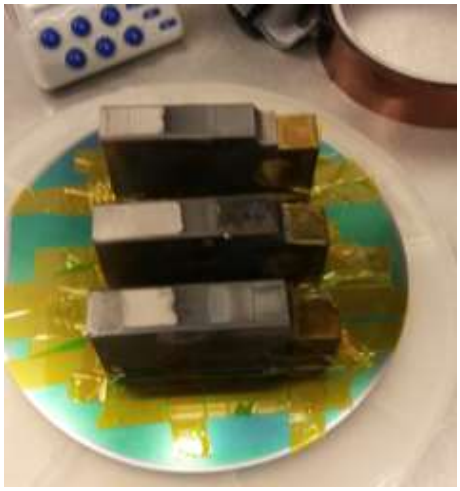

The process of Ni deposition took six hours for pump down to an acceptable level of vacuum, and then the Ni was deposited that took about an hour to deposit a Ni layer that was 2500 Å thick, and finally the pump up to atmospheric air took about fifteen minutes. The deposition of the Ni on the oxide also causes the samples to heat up, but only to at most 40°C which is not significant to alter the oxide. All indications are that e-beam evaporation is the best method for depositing Ni coating on the oxide. The other methods involve electrolytic nickel plating or electroless nickel plating, which use chemicals with possible consequences of affecting the oxide characteristics. The only downside to the e-beam evaporation method is the possible diffusion of Ni into the oxide; however, this is insignificant due to all of the material having the same amount of Ni applied to the oxide and only approximately one hour of exposure. Therefore, if the oxide did penetrate the oxide then the amount of penetration should be consistent between each sample.

B.vi) Measurement of Oxide Profiles and Thicknesses

B.vi)(a) SEM Overview

Oxide thickness measurements and the characterization of its profiles as well as analysis of the oxide composition was performed using a scanning electron microscope (SEM). The SEM used was a FEI Nova Nanolab 200 Dual-Beam Workstation located in the Arkansas Nano & Bio Materials Characterization Facility. An example of such a measurement is shown in Figure 27 for a C(T) specimen.

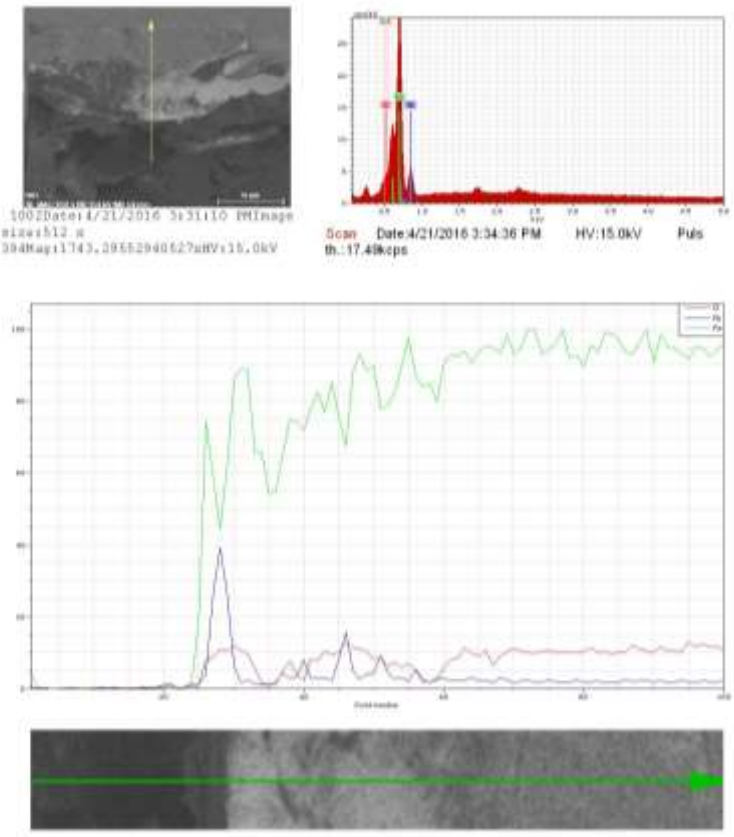

Figure 27 – SEM analysis of the side profile of a fractured C(T) specimen.

Going clockwise from the top we see the SEM picture of the oxide, followed by composition spectrum, the chemical composition profile, along the fracture surface.

The problem with the analysis in Figure 27 results from the electrons bouncing off the rough fracture surface of the C(T) specimens making it harder to decipher the oxide thickness as illustrated in Figure 28.

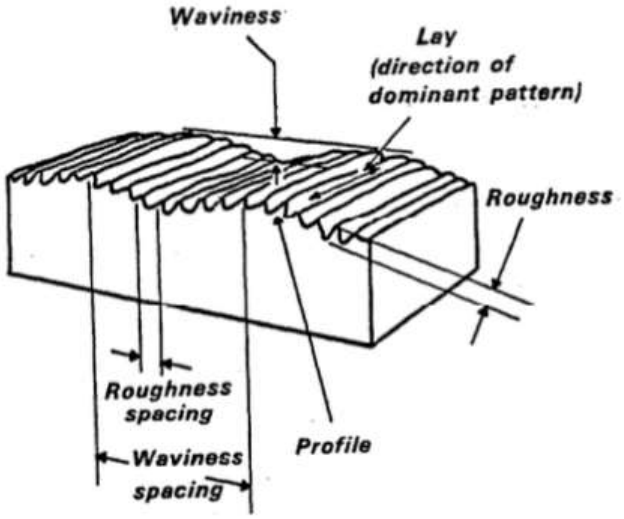

Figure 28 – Polished Surface and Fractured Surface [19]

To resolve this problem, an epoxy resin was applied to the fracture surface to provide a continuous surface past the edge of the sample that shows up as a black surface seen in the top left picture in Figure 29. The SEM machine used is also equipped with the ability to perform energy-dispersive X-ray spectroscopy or EDX as shown in Figure 29.

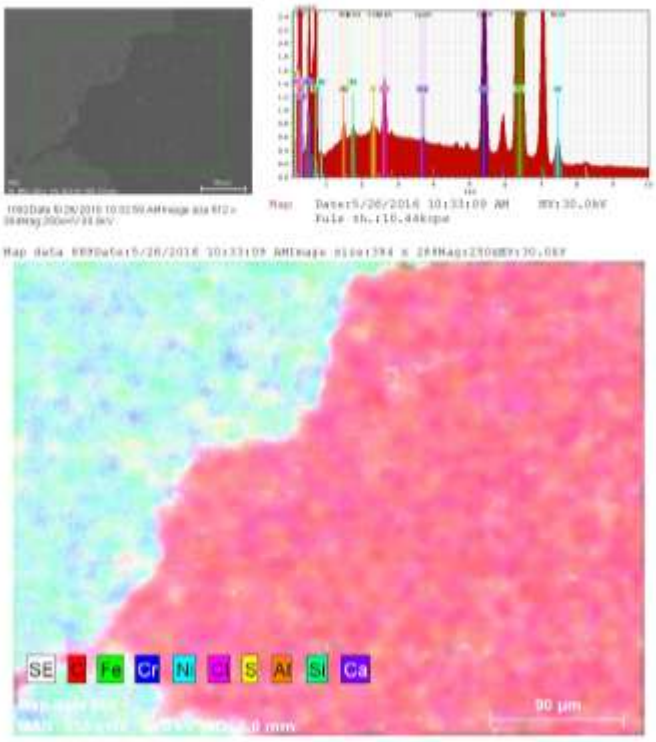

Figure 29 – SEM of Fractured Surface with Epoxy Coating

B.vi)(b) Sample Preparation

The application of the epoxy to the samples involves placing the samples in the epoxy hardening container, shown in Figure 30, and allowing the epoxy to harden for at least 24 hours. After the epoxy has hardened the samples are removed from the epoxy hardening container and cut to show the surface of interest.

Figure 30 – Epoxy Hardening Container with Sample

The samples were polished after being sectioned in order to increase the possible resolution of the SEM. The sequence of polishing the samples for SEM analysis is the following:

1. Clean sample from contaminates with Acetone
2. Start with 200 Grit Paper
3. Intermitted cleaning with Acetone
4. Move to 400 Grit Paper
5. Intermitted cleaning with Acetone
6. Move to 800 Grit Paper
7. Intermitted cleaning with Acetone
8. Move to 1200 Grit Paper
9. Clean the sample again with Acetone

The roughness of the samples to a high degree affects the resolution of the picture during SEM analysis due to electrons bouncing off the surface at an angle away from the collector. Polishing on the sectioned surface exposes the oxide surface as shown in Figure 31. The material from top to bottom of Figure 31 is Epoxy, Ni coating, oxide, parent material, oxide, Ni, and then Epoxy. The polishing of the samples also needs to have the direction of the polishing rotated 90 degrees [18] with each increasing size of grit as shown in Figure 31. The benefit of this method comes from the being able to have a visual indication when the sample has been polished to the roughness of the polisher.

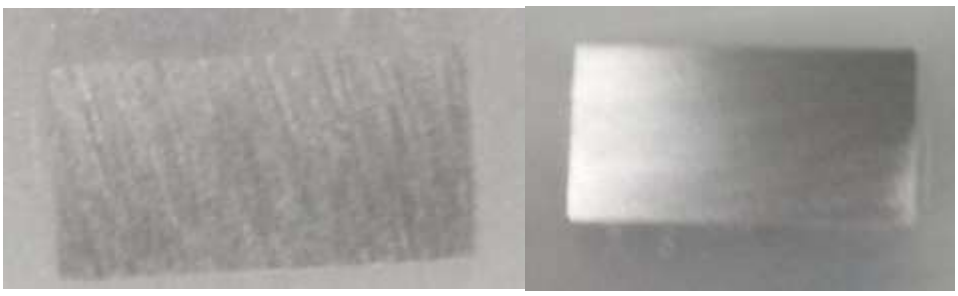

Figure 31 – Sample Polishing with Rotation

Due to the nonconductive behavior of the epoxy, a Ni conductive filler material was added to the epoxy to assist with flow of electrons in the SEM to the ground. Figure 32 shows the differences between the SEM pictures with and without the conductive filler.

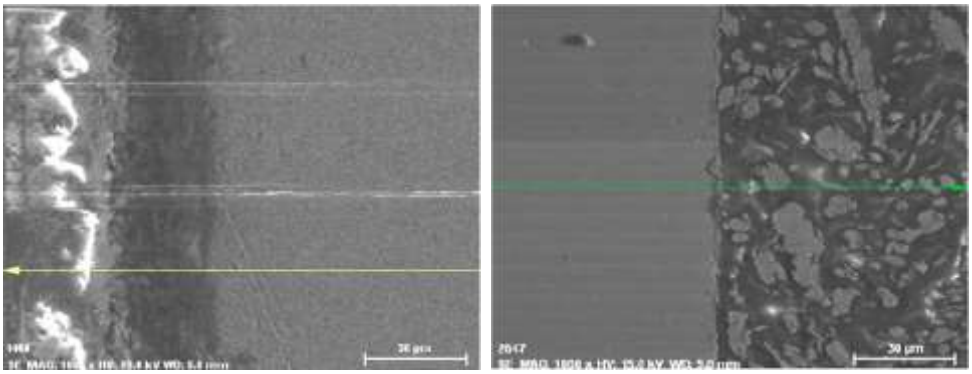

(a) (b)

Figure 32 - Difference Between SEM Output with and without Filler Material
(a) Without Conductive Filler (b) With Conductive Filler

The final preparation of sample for the SEM chamber involves placing a copper conductive tape to connect or "wire" the sample material to the ground of the SEM machine. Figure 33 shows how the sample is completely prepared for the SEM.

Figure 33 - C(T) Sample Prepared for SEM with Copper Conductive Tape

B.vi)(c) Procedure During SEM

The procedure devised to measure the oxide thickness in the oxidation samples is similar to that used for C(T) samples. First the SEM is through the initial setup procedures to bring itself into focus. Next the stage controls, Figure 34, of the SEM are used to locate the long surfaces of

interest for both the oxidized samples and the C(T) specimens, which is the top surface of Figure 33 for a C(T) sample.

The next step is dependent on if it is the oxidized sample or a C(T) sample being analyzed. For the oxide samples, the next steps were devised to collect data as near to the center of the sample's oxide edges to minimize influence from the corners. The SEM stage control has the capability of moving to points on the surface of the sample with increments down to 0.0001 mm as shown in Figure 34.

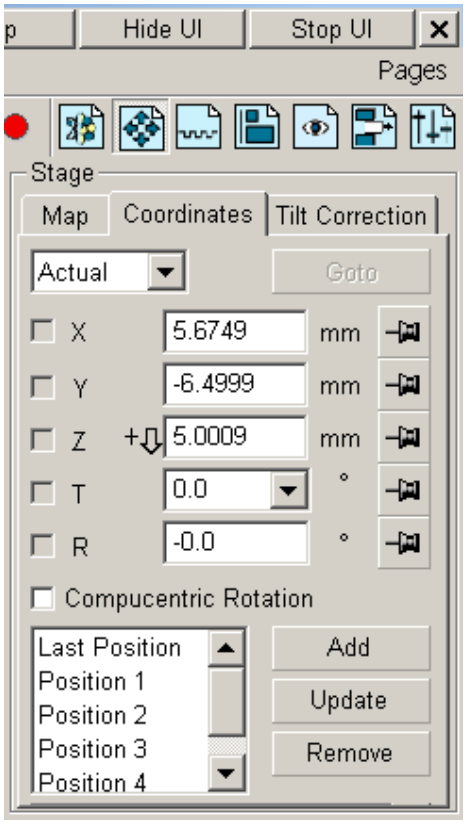

Figure 34 – SEM Sample Stage Movement Control

The center point can be found by measuring the location using the x and y stage movement controls referenced to the two corners. The final step for the oxide sample is to take nine EDX measurements with four points taken in 0.5 mm increments above and below the center point of the sample.

The process of measuring the oxide thickness after finding the surface of interest for the C(T) sample involves locating the beginning and end points of the creep-fatigue crack surface. The oxide thickness between the beginning and end points of creep-fatigue crack growth were measured in 0.5 mm increments using the EDX.

B.vi)(d) Procedure for Analyzing SEM Photomicrographs

The analysis of the SEM photomicrographs is done in MATLAB© using it's imtool. The necessary steps to open the image in the imtool are shown in Figure 35, which is achieved by calling the imtool as a function with the input of the image file to analysis.

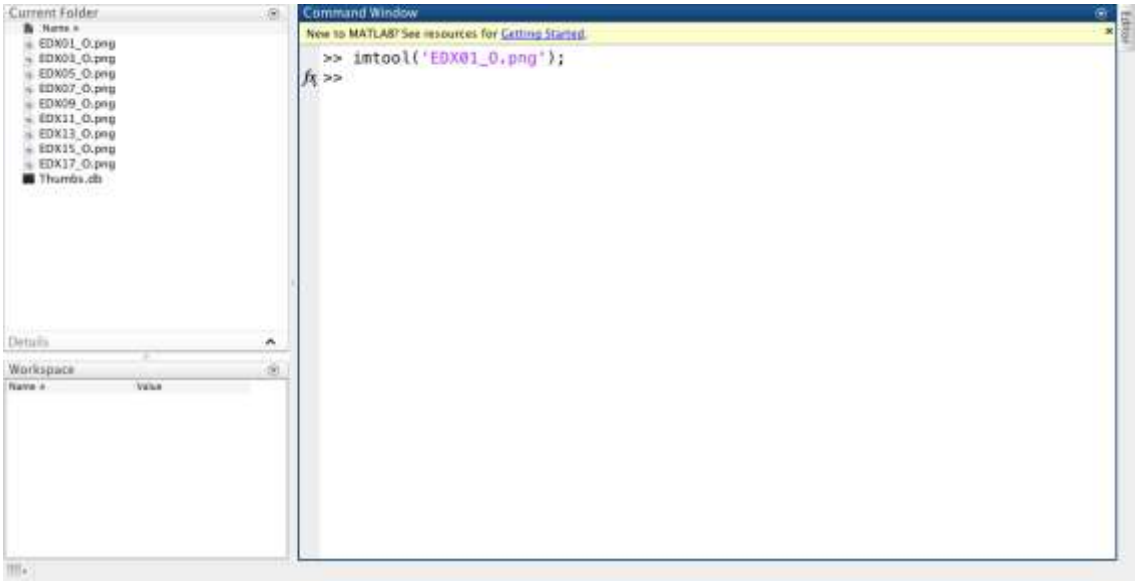

Figure 35 - MATLAB© Command Window to Pull Images into imtool

The result of Figure 35 is a new window shown in Figure 36. Figure 36 shows the EDX output of the SEM, which is a map of location of oxygen on the sample's surface. The difference in brightness or luminosity of Figure 36 is an indication of the oxygen content at a location. Therefore by using the difference in luminosity of Figure 36 the oxide is easy to find, being the lighter green content in the center. Another feature of the imtool is an icon on the imtool toolbar that allows the measurement of pixel distance as shown in Figure 37. Once clicked on, the

cursor turns into a plus sign that allows you to hold and drag it to the opposite side of the oxide to show the pixel distance between the edges of the oxide. The output a single distance measurement is shown in Figure 38.

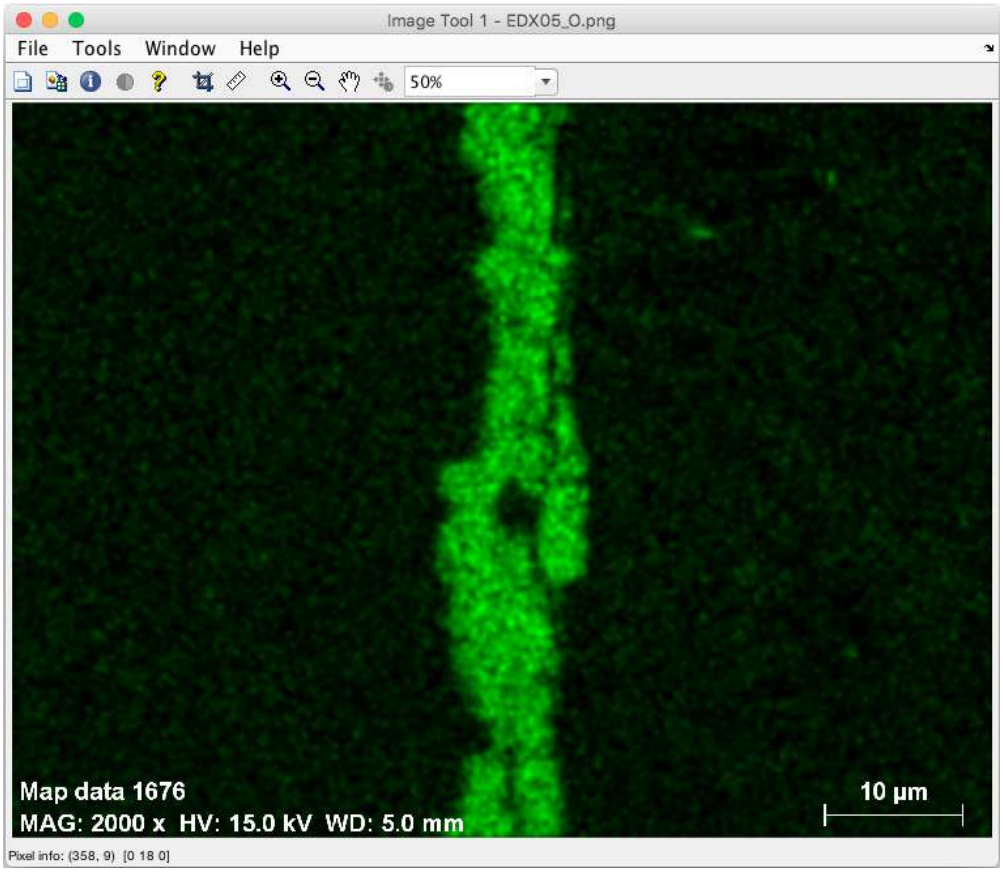

Figure 36 - imtool on an EDX SEM Image

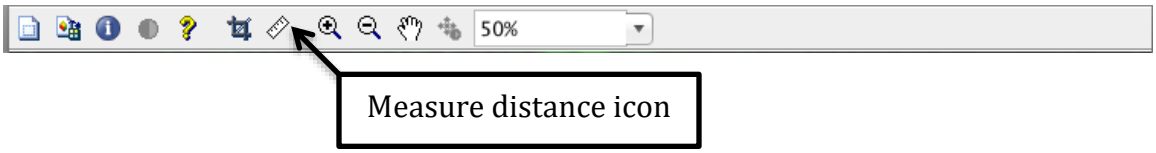

Figure 37 - imtool Toolbar

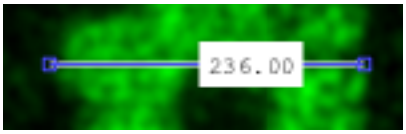

Figure 38 - Zoomed in Output of Measure Distance Icon

The advantage of this process comes from finding the pixel to length ratio from the scale in the bottom right corner of Figure 36. Using the pixel to length ratio the pixel distance of multiple

measurements, as shown in Figure 39, can be converted and averaged to find the oxide thickness at this location.

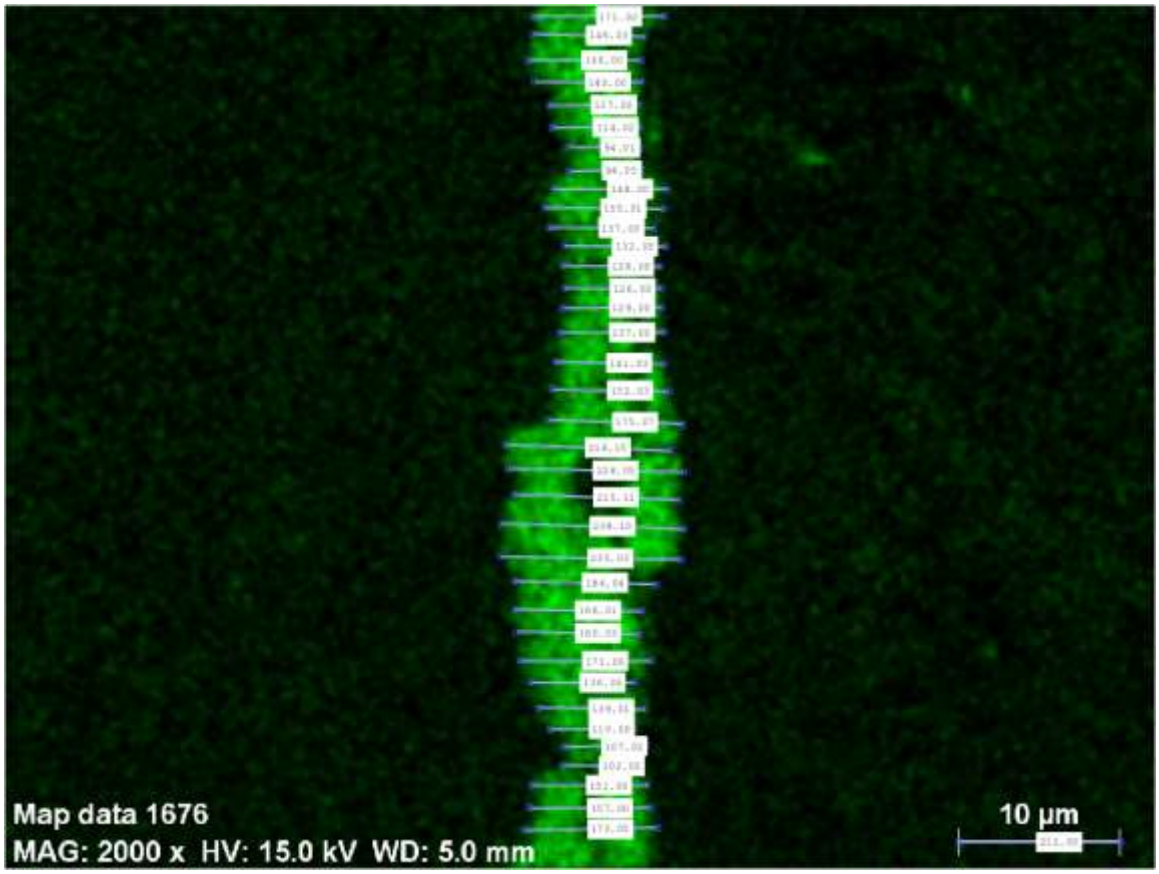

Figure 39 - Output for One Location using MATLAB©'s imtool

The only downside to this method is this is a manual edge detection method that relies on the user to click and drag to find the distance. To try and elevate this in a more automated approach, MATLAB©'s edge detection was used to alleviate this. Figure 66 shows an output applied using different tolerances. The results of using MATLAB©'s edge detection where not satisfactory to create a method of finding the distance between points and was therefore abandoned. However, if successful edge detection software was applied ability and speed of calculating the oxide thickness should increase.

V. Data Analysis

A. Determination of Parabolic Constant, k_p, for Mass Gain

The weight gain of samples from this experiment and from the literature [15] is shown in Figure 40. The results at 600 C in the literature and from this experiment are in very good agreement.

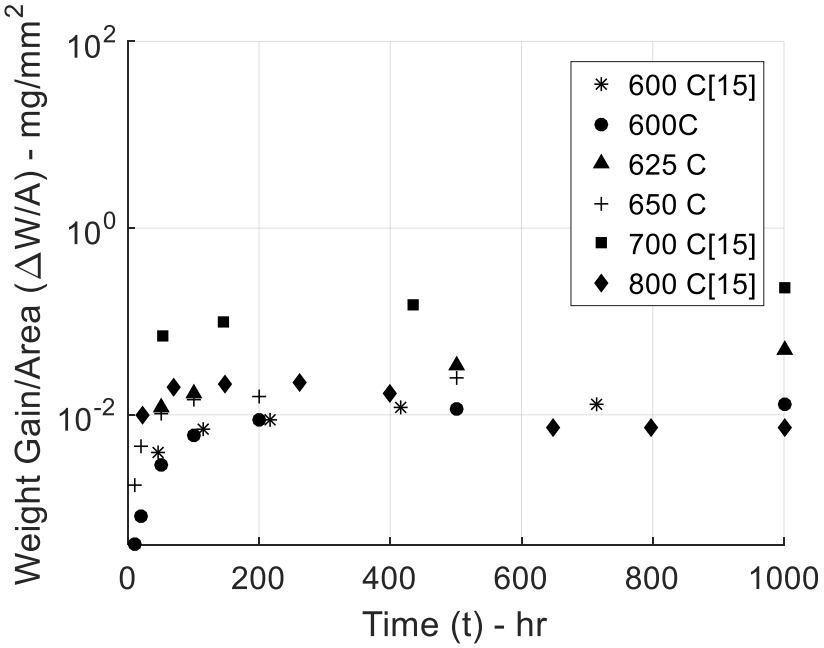

Figure 40 – (Weight Gain/Area) vs Time all Data Points

Figure 41 shows how a linear curve fit can be used to find the parabolic weight gain constant, K_p, by plotting the weight squared versus time. The data points pulled from the plots for 600 C P91 steel in the literature [15] versus this experiment result in a percent difference of 3.11%, which indicates the results are in reasonable agreement from different studies. The curve fits found in Figure 41 are a linear fit of the following,

$$\left(\frac{\Delta W}{A}\right)^2 = K_p * t \tag{22}$$

where the K_p values for each curve fit are in Table 5. The reason the linear fit is not allowed to have a y-intercept value is initially the weight gain value should be zero.

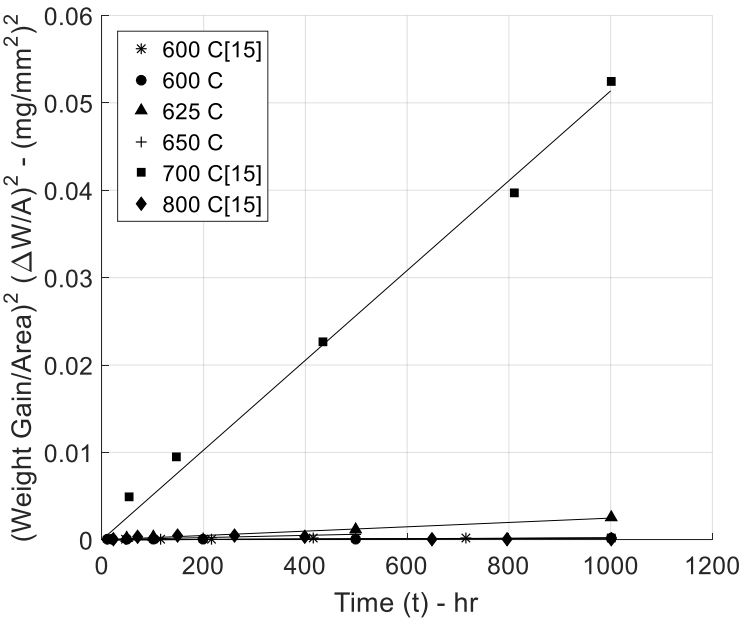

Figure 41 – (Weight Gain/Area)^2 vs Time to Find K_p Values

Table 4 – K_p for finding Weight Change/Area

Temp - C	K_p – mg^2/(mm^4*hr)
600	2.25E-07
600*	1.897E-07
625	2.48E-06
650	1.271E-06
700*	5.14E-05
800*	**2.05E-07**

* Data pulled from Mathiazhagan and Khanna[15]

Comparing the values from Table 4 pulled from Mathiazhagan and Khanna[15], shown in Table 5, are in agreement except for 800 C.

Table 5 – K_p for finding Weight Change/Area from Literature[15]

Temp - C	Kp – mg^2/(mm^4*hr)
600	2E-7
700	5E-5
800	**0.5E-3**

The difference in K_p for the 800 C of 2.05E-7 vs 0.5E-3 is most probably due to not being able to account for volatilization and/or spallation in the samples. Figure 42 shows the correlation

between K_p and temperature using data from this experiment and the values reported in the literature.

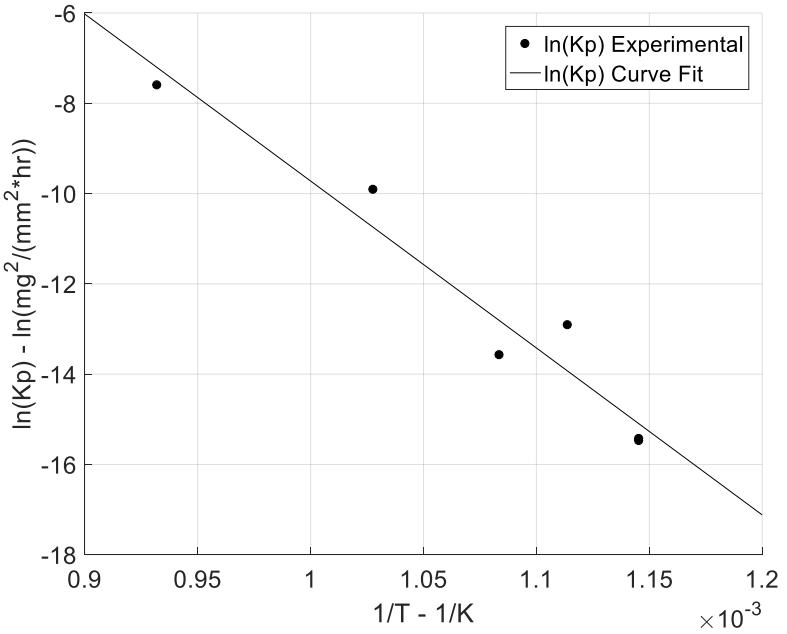

Figure 42 – Ln(K_p) versus 1/Temperature

The curve fit does correlate with the idea of oxide kinetics being a diffusion-controlled process; therefore Eq. 15 can be used as a guide to develop a relationship between K_p and temperature as,

$$\ln(K_P) = \ln\left(K_{p,0}\right) - \frac{Q}{RT} \tag{23}$$

which leads to the following,

$$K_p = K_{p,0} * \exp\left(-\frac{Q}{RT}\right) \tag{24}$$

The divergence from the parabolic model happens at 800 C due to volatilization and/or spallation and at 650 C what appears stronger passivation than predicted by the model.

The stronger passivation at 650 C can be model by adding another term to the parabolic model as,

$$\frac{\Delta W}{A} = \sqrt{K_p * t} + c_0 * t^{c_1} \quad (25)$$

where c_0 and c_1 are curve fit constants from the data. The first step in using model created by Eq. 25 is to find the divergence from the parabolic mode, 650 C is after the first four data points shown in Figure 43.

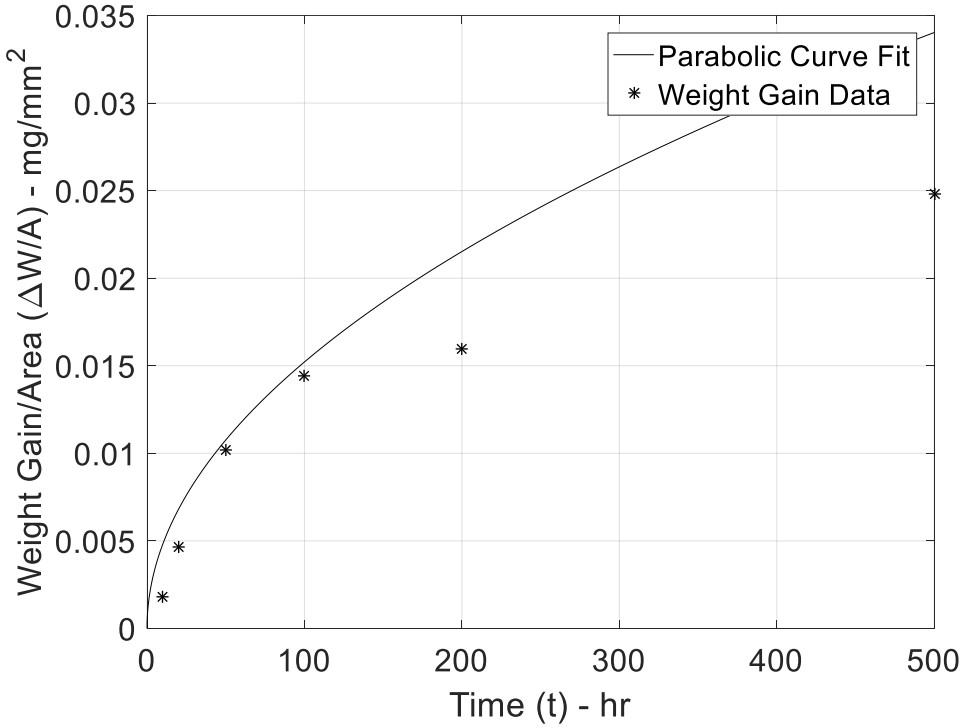

Figure 43 – Divergence from Parabolic Model for Weight Gain at 650 C

The parabolic constant can then be found by using the first four data points with the parabolic model and is tabulated in Table 6 using the linear fit from Eq. 22.

Table 6 – Weight Gain Parabolic Constant using First Four Data Points

Temp - C	K_p – mg^2/(mm^4*hr)	$\left({}^{\Delta W}/_{A}\right)_0$ – mg^2/mm^4
650	2.32E-6	-1.985E-5

Next, Eq 25 is used as a model inputted into Matlab©'s Curve Fit Tool's custom equation to find the constants c_0 and c_1, which are shown in Figure 44 and tabulated in Table 7.

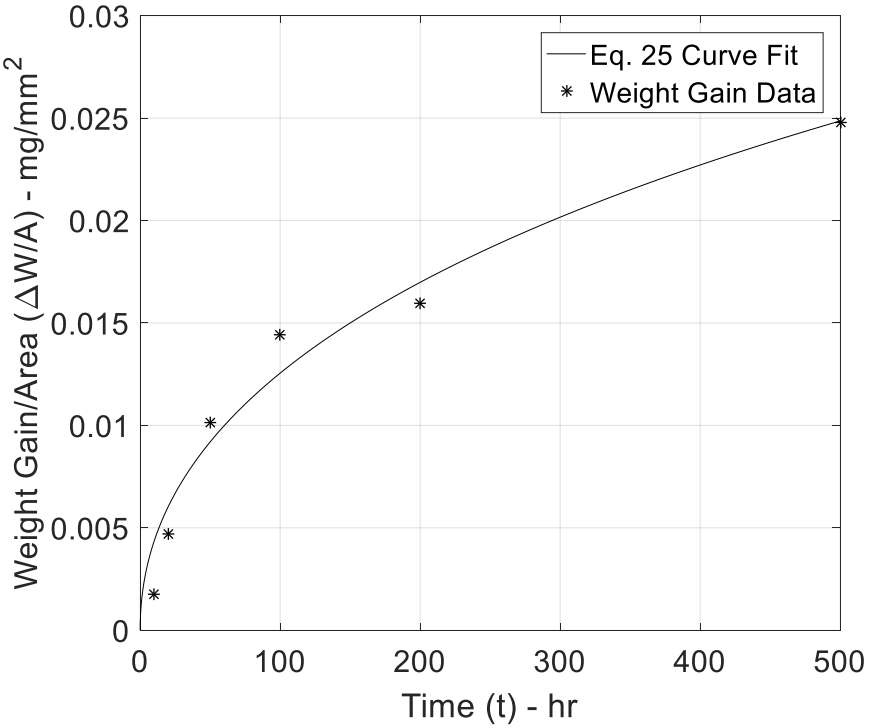

Figure 44 – Weight Gain at 650 C using Eq. 25

Table 7 – Weight Gain Parabolic Constant using First Four Data Points

Temp - C	c_0 - mg^2/(mm^4*hr)	c_1
650	-7.78E-05	0.767

Since the effects of stronger passivation at 650 C have been removed from K_p, the K_p value tabulated in Table 6 will be used for further data analysis. Figure 42 can be redrawn with the K_p value at 650 C in Table 6 to show the relationship between K_p values following the parabolic model and temperature.

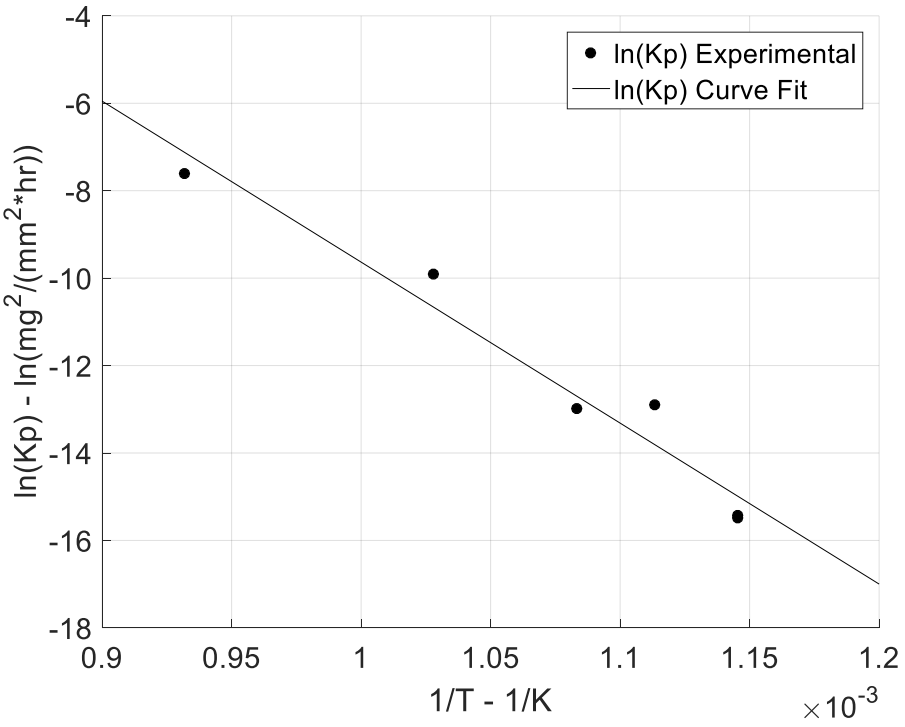

Figure 45 – Figure 42 redrawn with updated K_p For 650 C

Since the applications of the oxide thickness involve exposure temperatures of about 600 C, the modeling will focus in the range of 600 to 650 C for which we have oxidation thickness data in addition to the weight gain data. When looking into the 600 C through 650 C range the curve fit, shown in Figure 46, shows considerable scatter between the fit and the experimental values. This is primarily due to anomaly in the 650 C data showing a sudden decrease in the K_p value for unexplained reasons. Therefore, a weight gain relationship between temperatures of 600 C to 625 C will also derived, also shown in Figure 46.

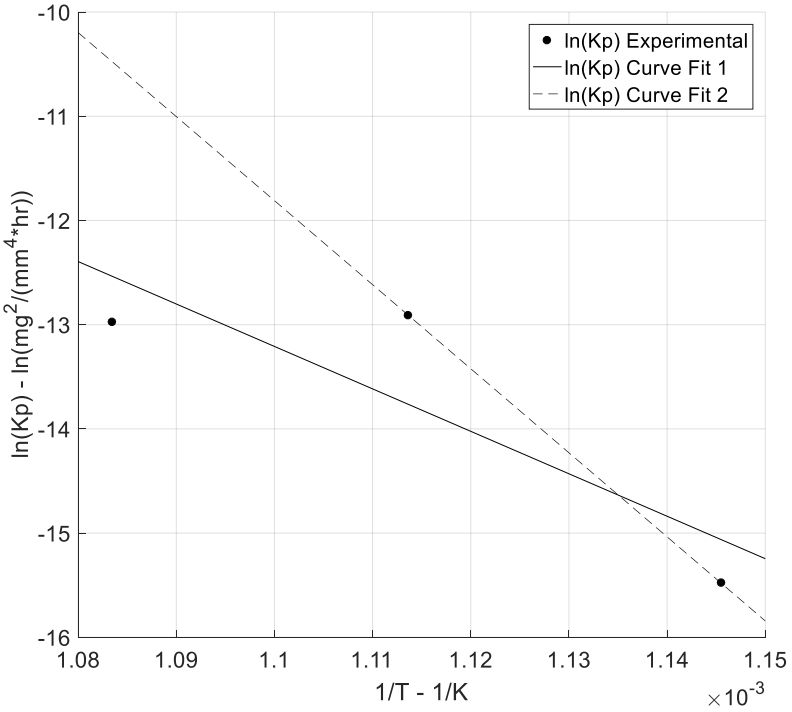

Figure 46 – $\ln(K_p)$ for weight gain versus 1/Temperature

The curve fit values using Eq. 23 from Figure 46 are tabulated in Table 8, which has the activation energy and initial parabolic constant using the gas constant R in units of kcal/(K*mole).

Table 8 – Constants of Arrhenius type Equation for Weight Gain

Temperature Range - C	600 – 650	600 – 625
Q - kcal/mol	81.0	160.3
$ln(K_{p,0})$- ln(mg^2/(mm^4*hr))	31.6	76.9

Finally the relationship of weight gain and temperature and time can be collected together to form,

$$\frac{\Delta W}{A}(T,t) = \sqrt{K_{p,0} * \exp\left(-\frac{Q}{RT}\right) * t} \tag{26}$$

B. Oxide Growth Measurements

Oxide thickness over time is shown in Figure 47 with the error bars indicating the standard deviation above and below the average. The average coefficient of variation of the error bars in

Figure 47 is 0.306 or about 30.6%. Another point of interest in Figure 47 is the data at 625 C for 1000 hrs and 600 C at 500 hrs, which seem to diverge from the parabolic trend.

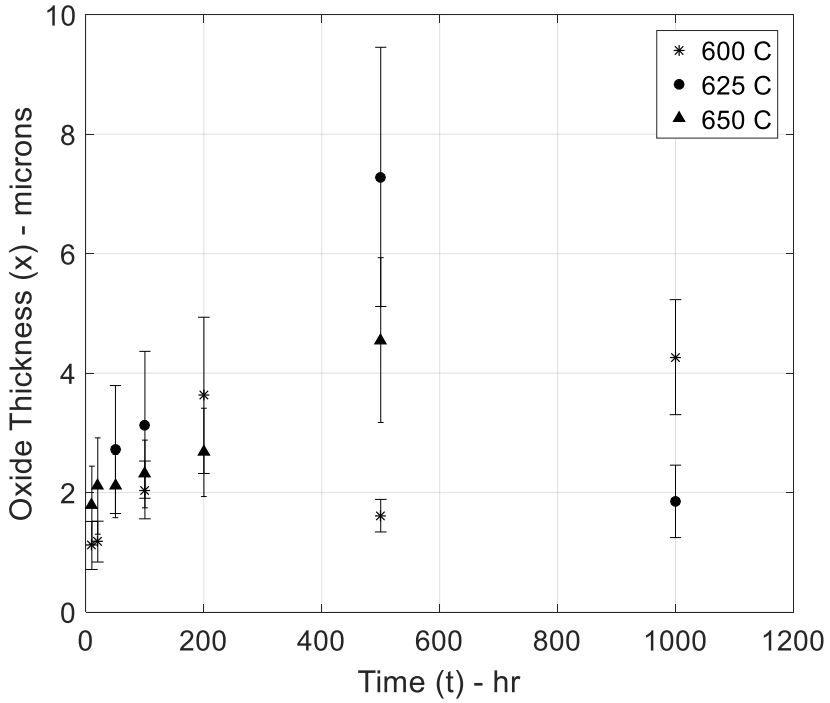

Figure 47 – Oxide Thickness vs Time

Figure 48 and 49 are the oxide thickness squared versus time, which have the following behavior,

$$X^2 = K_p * t \tag{27}$$

By plotting this the parabolic growth constant can be found as the slope of the curve, which is documented in Table 9.

Table 9 – K_P for oxide thickness

Temperature - C	K_P – microns^2/hr
600	1.738E-2
625 with 1000 hrs	2.48E-2
625 without 1000 hrs	1.063E-1
650	4.18E-2

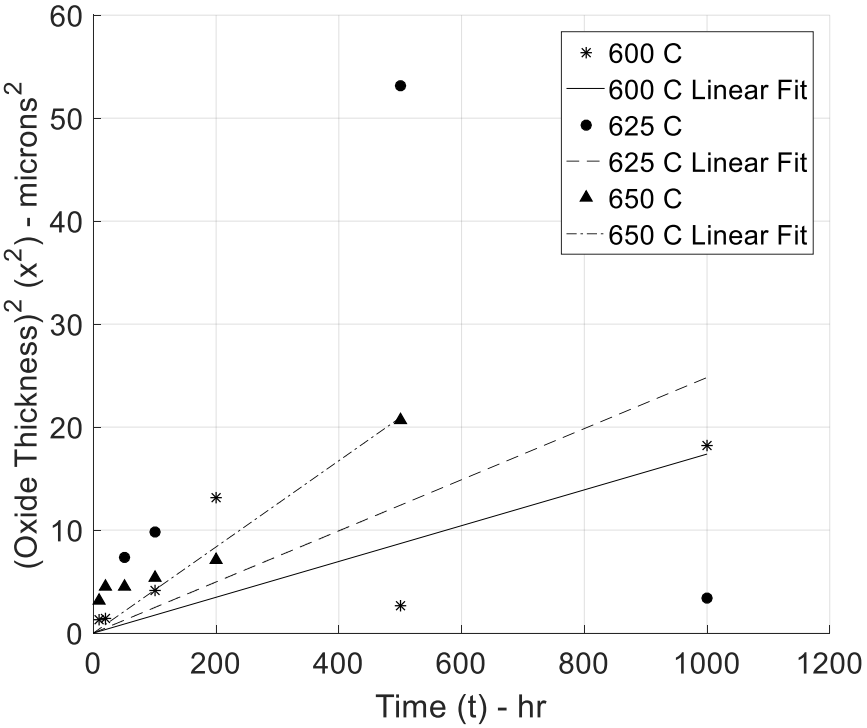

Figure 48 – (Oxide Thickness)^2 vs Time

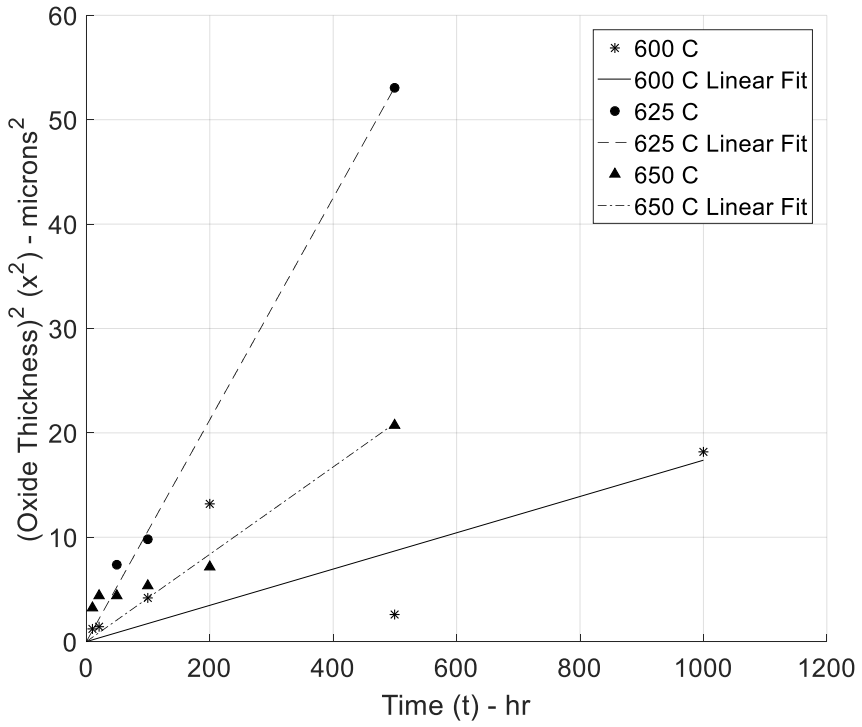

Figure 49 – (Oxide Thickness)^2 vs Time without 625 C 1000 hr

Figure 48 and 49 for 650 C shows a divergences in behavior after the second data point instead of the forth data point as with the weight gain. Therefore, oxide thickness at 650 C will use the first two data points to find the k_P value of Eq. 25 shown in Figure 50 and Table 10.

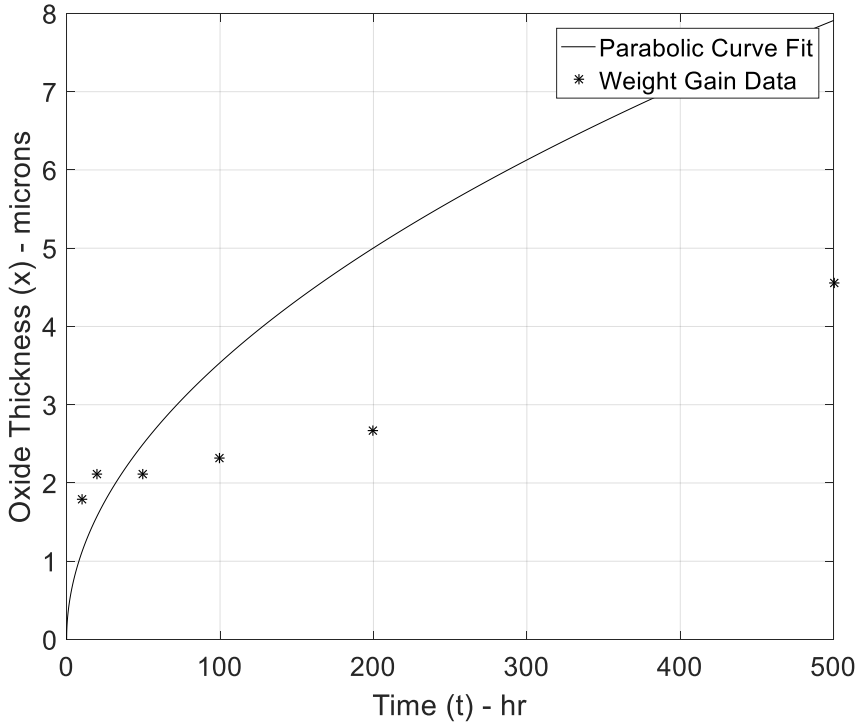

Figure 50 - Divergence from Parabolic Model for Oxide Thickness at 650 C

Table 10 – K_P for Oxide Thickness at 650 C using First Two Data Points

Temperature - C	K_P – microns^2/hr	${X_0}^2$ – microns^2
650	1.251E-1	1.947

Eq. 25 is employed again using Matlab© Curve Fitting Tool's custom equation capabilities to find values for c_0 and c_1, which are tabulated in Table 11 and shown in Figure 51.

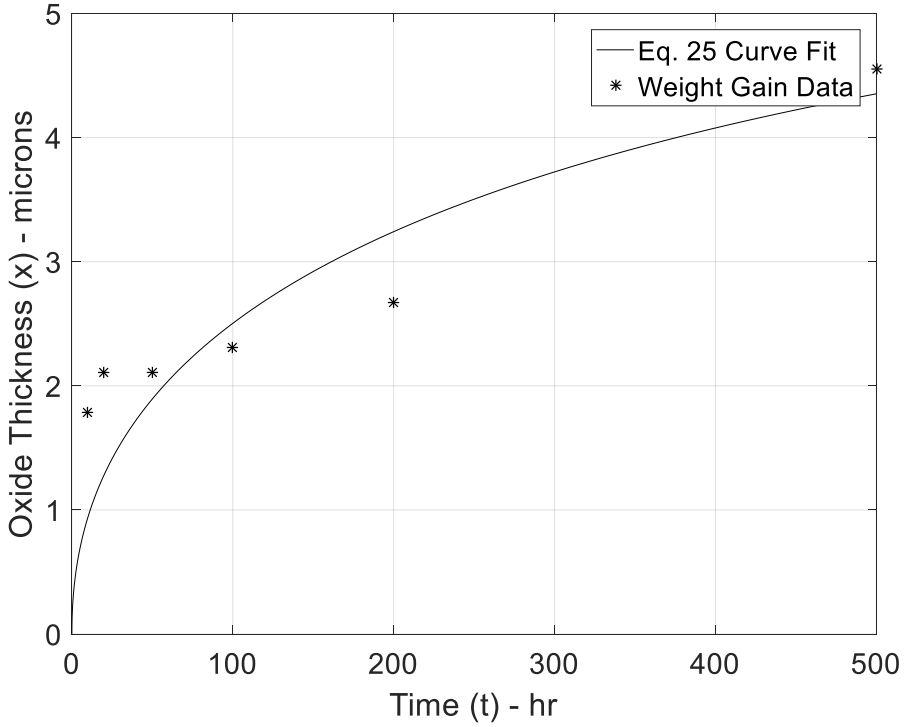

Figure 51 – Oxide Thickness at 650 using Eq. 25

Table 11 – Weight Gain Parabolic Constant using First Four Data Points

Temp - C	c_0 - microns^2/(*hr)	c_1
650	-2.32E-2	0.812

The oxide thickness k_P at 650 C will in all further analysis will be the value in Table 10 due to the passivation effect being removed from the term. Figure 52 contains the relationship between k_P and temperature with 650 C and without 650 C respectively.

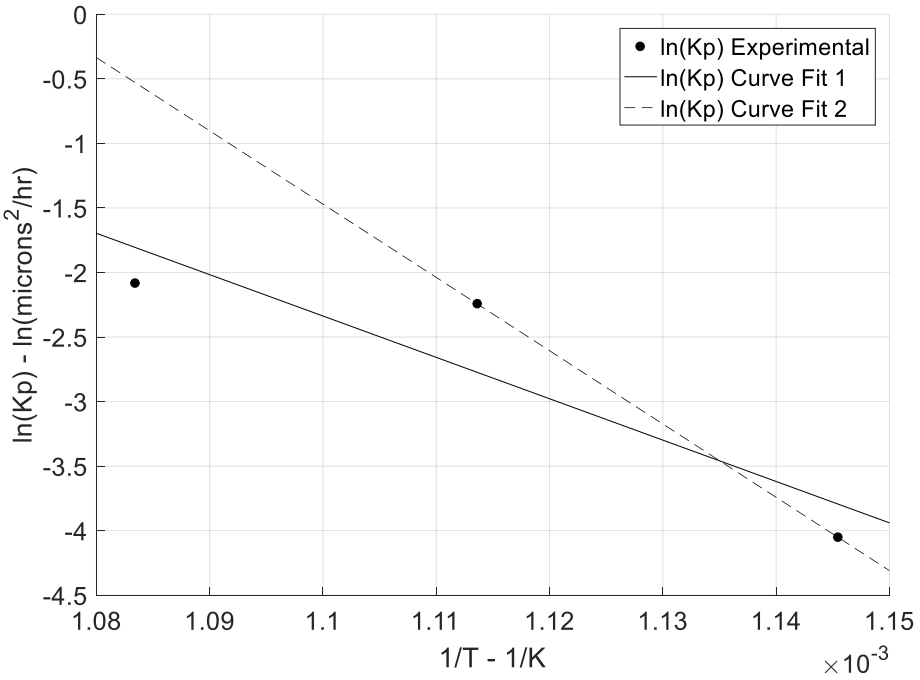

Figure 52 – ln(K_P) for Oxide Thickness vs Temp^-1

The K_P and temperature relationship in Figure 52 can be developed into a model exactly like Eq. 23 for Weight Gain leading to,

$$K_p = K_{p,0} * exp\left(-\frac{Q}{RT}\right) \tag{28}$$

where the Q and $K_{p,0}$ values for oxide thickness are documented in Table 12.

Table 12 – Constants of Arrhenius type Equation for Oxide Thickness

Temperature Range - C	600 - 650	600 - 625
Q – kcal/mol	63.7	112.8
ln($K_{p,0}$) – microns^2/hr	32.9	61.0

The result relationship of oxide thickness with temperature and time is,

$$x(T,t) = \sqrt{K_{p,0} * \exp\left(-\frac{Q}{RT}\right) * t} \tag{29}$$

Since all of the oxides are similar the activation energy found should be approximately equal, the activation energy values in Table 8 should be approximately equal to the values in Table 12 with the values comparison shown in Table 13.

Table 13 – Activation Energy Values

	Q – kcal/mol
Figure 46, 600 – 650 C	81.0
Figure 46, 600 – 625 C	160.3
Figure 52, 600 – 650 C	63.7
Figure 52, 600 – 625 C	112.8

The activation energies tabulated in Table 14 show are activation energies found in Young's book[13]. The first two are from self-diffusion of Cr in a binary alloy of Cr-Fe(γ) and Cr-Fe(α), and the third value is the diffusion activation energy of Cr in Cr_2O_3.

Table 14 – Comparable Activation Energy Values[13]

Type	Q – kJ/mol
Self-diffusion of Cr in Cr-Fe(γ)	263.9
Self-diffusion of Cr in Cr-Fe(α)	250.8
Diffusion of Cr in Cr_2O_3	330

Upon inspection of the values in Table 14 and converting the values of Table 13, the correlation between the activation energy of Figure 46 from 600 – 650 C and the Diffusion of Cr in Cr_2O_3 along with the similarities between the activation energy of Figure 52 from 600 – 650 C and the self-diffusion of Cr in Cr-Fe(γ) and Cr-Fe(α) points towards using the activation energy in the 600 – 650 range can be seen in Table 15.

Table 15 – Comparison of Activation Energies

Type	Q – kJ/mol
Self-diffusion of Cr in Cr-Fe(γ) [13]	263.9
Self-diffusion of Cr in Cr-Fe(α) [13]	250.8
Figure 52, 600 – 650 C	267
Diffusion of Cr in Cr_2O_3 [13]	330
Figure 46 – 600 – 650 C	339

Another implication of the activation energies of the temperature range 600 – 650 C being similar is the assessment the controlling process being diffusion, which gives more credence to the parabolic model. Since the activation energies between the Arrhenius oxidation and weight gain models should be similar, the decision to use an average of the activation energies. Table

16 contains the averaging of the activation energies obtained from figure 46 and 52 with a comparison of the averaging of the self-diffusion of Cr in Cr-Fe(γ) and diffusion of Cr in Cr_2O_3.

Table 16 – Comparing Activation Energy Values

	Q – kcal/mol	Percent Difference - %
Figure 46, 600 – 650 C,WG	81.0	11.88%
Figure 52, 600 – 650 C,OT	63.7	12.72%
Average	72.4	
Self-diffusion of Cr in Cr-Fe(γ) [13]	63.1	11.79%
Diffusion of Cr in Cr_2O_3 [13]	78.9	10.54%
Average	71.0	

Comparing the averages of Table 16 results in a percent difference of less than 1%, and the activation energy found from Figure 45 is also in agree with the Q_{AVG} found being 73 kcal/mol.

The weight change per area's and oxide thickness's activation energy being similar is important due to the oxide thickness and weight should having the following relationship,

$$\Delta x \propto \left(\frac{\Delta W}{A}\right) \tag{30}$$

where Δx is the increase in oxide and $\frac{\Delta W}{A}$ is the weight change per surface area. The literature [13] shows that the oxide and weight change per surface area relationship is the following,

$$x = \frac{1}{16\rho_s'}\left(\frac{\Delta W}{A}\right) \tag{31}$$

where ρ_s' is the density of the scale or oxide in this case. The one-sixteenth constant in the equation is derived from the following chemical equation,

$$\frac{x}{y}M + \frac{1}{2}O_2 \rightarrow \frac{1}{y}M_xO_{\square} \tag{32}$$

where x and y are coefficients to balance out the chemical equation for a metal. The one-sixteenth term comes from stoichiometric considerations during the oxidation reaction and can be lumped into a single constant,

$$\rho_s = 16\rho_s' \tag{33}$$

Therefore using Eq. 31 and 33, the density of the oxide can be modeled by,

$$\rho_s = \frac{1}{x(T,t)}\left(\frac{\Delta W}{A}(T,t)\right) \tag{34}$$

Inputting the oxide thickness and weight gain model into the above equations results in,

$$\rho_s = \sqrt{\frac{K_{p,O_{WG}}}{K_{p,O_{OT}}} * \exp\left(\frac{Q_{WC}-Q_{OT}}{RT}\right)} \tag{35}$$

where WC signifies weight change and OT signifies oxide thickness. The Q_{WC} and Q_{OT} are both taken as the average activation energy value derived from the two methods thus leading to,

$$\rho_s = \sqrt{\frac{K_{p,O_{WG}}}{K_{p,O_{OT}}}} \tag{36}$$

and,

$$x(t) = \frac{\sqrt{K_{p,0_{WG}} * \exp\left(-\frac{Q_{AVG}}{RT}\right) * t}}{\rho_s} \tag{37}$$

In order to achieve the above relationship using Q_{AVG} the $K_{p,0}$ values for weight gain and oxide thickness will have to be retained using the Q_{AVG}. The method chosen to find the $K_{p,0}$ is using Curve Fitting Tool within Matlab because this allows the user to input custom equations. The result of applying this method is seen in Figures 53 and 54, with the resulting curves tabulated in Table 17.

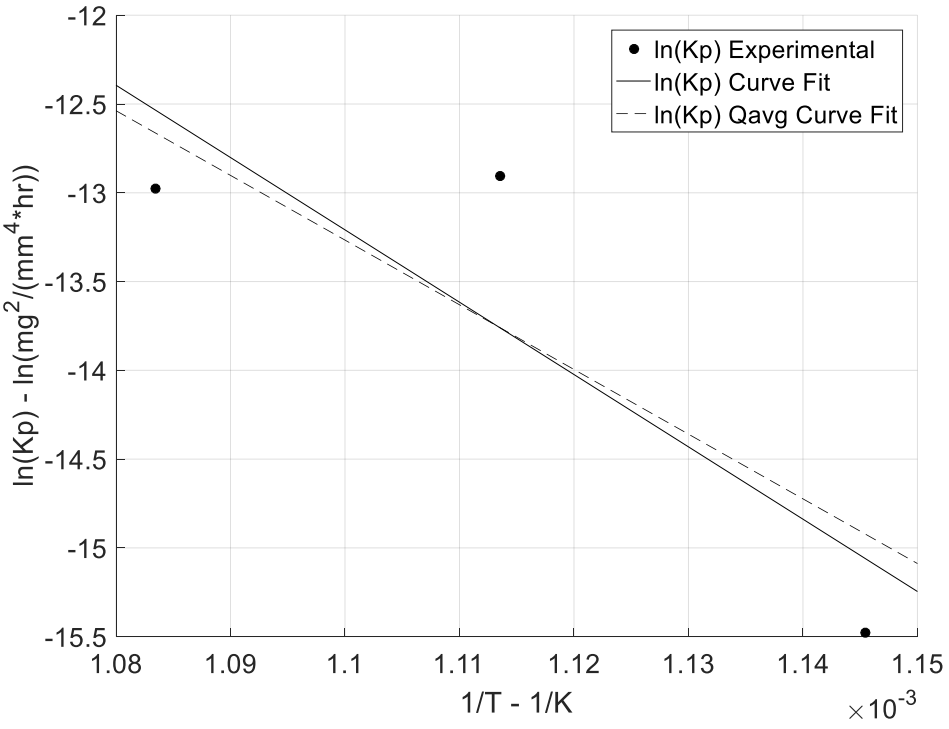

Figure 53 – Weight Gain ln(Kp) using Qavg versus Qwg for 600, 625, and 650 C

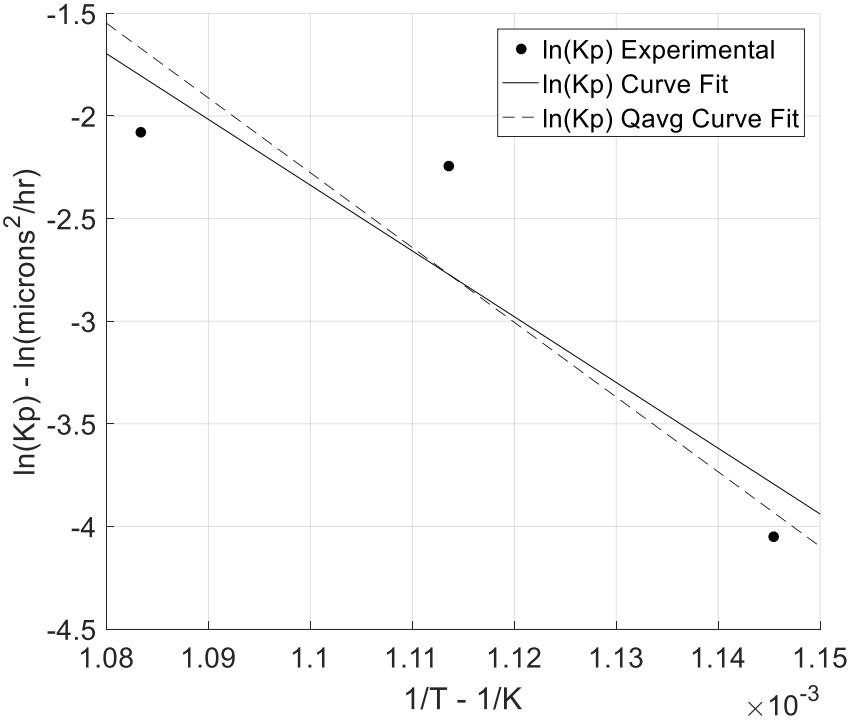

Figure 54 – Oxide Thickness ln(Kp) using Qavg versus Qwg for 600, 625, and 650 C

Table 17 – Coefficients of Qavg Curve Fit

Figure	$a = -\frac{Q}{R}$	$b = \ln(K_{p,0})$
53	-3.64E4	26.8
54	-3.64E4	37.8

Using the $\ln(K_{p,0})$ term found by using Q_{avg} the density constants, ρ_s and $\rho_s{}'$, can now be found by using Eq. 36.

Table 18 – Density Constant, ρ_s and $\rho_s{}'$ using Qavg

Temperature Range	ρ_s - mg/(mm^2*micron)	$\rho_s{}'$ - g/(cm^3)
600 – 650 C	4.09E-03	0.255

The density values can also be found by plotting the weight gain per area versus oxide thickness.

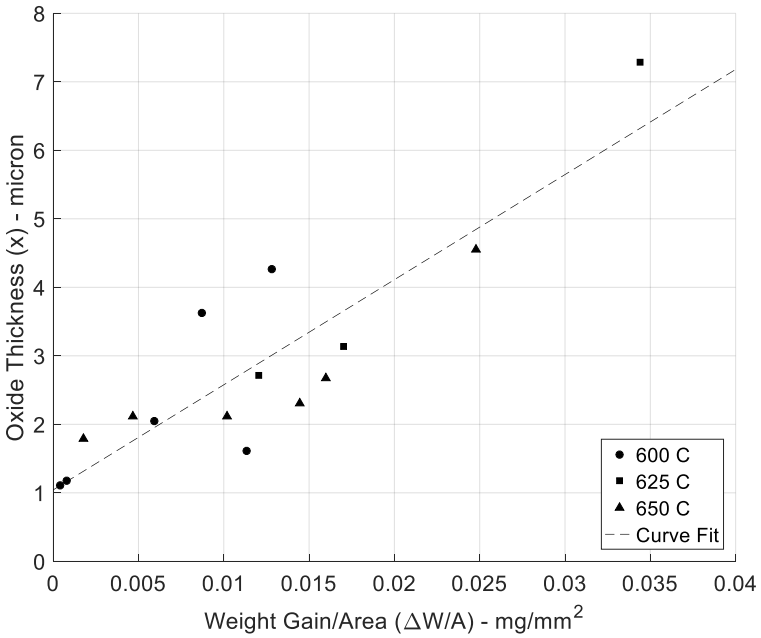

Figure 55 - Weight Gain/Area vs Oxide Thickness

Ideally the curve fit for Figure 55 would be,

$$x = c_0 \frac{\Delta W}{A} \tag{38}$$

since initially both oxide thickness and weight gain should be zero. However, accounting for the offset in Figure 55, the curve fit to find the density is,

$$x = c_0 \frac{\Delta W}{A} + c_1 \tag{39}$$

where the constants for Eq. 38 and 39 are tabulated in Table 19.

Table 19 - Constant for Eq. 38 from Figure 55

	c_0 – micron*mm^2/mg	$c_1 - micron$
Eq. 38	210.0	
Eq. 39	153	1.043

The density constant, ρ_s, and actual density, ρ_s', found by using Eq. 38 and 39 are tabulated in Table 20.

Table 20 – Density Values Calculated from Eq. 38 and 39

Eq. 38	
Density constant, ρ_s - g/(cm^3)	4.7612
Actual Density, ρ_s' - g/cm^3	0.298
Eq. 39	
Density constant, ρ_s - g/(cm^3)	6.5170
Actual Density, ρ_s' - g/cm^3	0.407

Comparing the actual density values in Table 18 and 20, the percent differences between the actual densities using Eq. 38 is 7.78% and Eq. 20 is 11.48%.

The percent differences of 7.78% and 11.48% are such due to how the actual density values are derived and can be considered acceptable. The actual density values found can be compared to stoichiometric density values of probable oxides on the samples, which can contain Fe_2O_3, Fe_3O_4, FeO, Cr_2O_3, and others when considering a Fe-Cr-O phase diagram[13]. The density of these oxides at 25 C can be found in Table 21 below, which have a higher value then found in Table 18 and 20.

Table 21 - Densities of Probable Oxides of P91 Steel[20]

Oxide Types	Density – g/cm^3
FeO	6.0
Fe_2O_3	5.25
Fe_3O_4	5.17
Cr_2O_3	5.22

The reason the density in Table 18 and 20 are higher then the oxides in Table 21 is due to the voids formed in the oxides during their growth. Finally, the different methods of calculating the

oxide thickness K_p value using Qavg can be compared with the measured K_p value from Figure 36 and Table 4, which are tabulated in Table 22 and 23.

Table 22 – Percent Difference Between Oxide Thickness K_p Values from Table 4 and Eq. 28 using Qavg values for Oxide Thickness from Table 15

	600 C	625 C	650 C
K_p Table 4	1.738E-2	1.063E-1	1.251E-1
K_p Eq. 28, 600 – 650 C	2.05E-02	6.54E-02	1.959E-01
Percent Difference	8.20%	23.85%	22.05%

Table 23 – Percent Difference Between Oxide Thickness K_p Values from Table 4 and K_p Values from Eq. 36, Eq. 28 using Qavg for Weight Gain from Table 15, and Density Constants

	600 C	625 C	650 C
K_p Table 4	1.738E-2	1.063E-1	1.251E-1
K_p Density Table 20, Eq. 38, and Table 17 for 600 – 650 C	1.457E-2	4.66E-2	1.397E-1
Percent Difference	17.62%	78.2%	11.03%
K_p Density Table 20, Eq. 39, and Table 17 for 600 – 650 C	7.73E-3	2.47E-2	7.42E-2
Percent Difference	76.85%	124.5%	51.1%

The reason the percent difference between the K_p values from Table 4 and K_p values calculated using density and Arrhenius K_p values from Table 17 in Table 22 are so high is due to the density value calculated through Eq. 39 incorporated an offset while the K_p values in using Eq. 38 do not. An issue arises from the large percent difference of K_p at 625 C because this value is used to find the crack growth rates. Due to the importance of the K_p value of 625 C being close to measured experimental value of K_p, the $\ln(K_{p,o})$ value used to calculate the Arrhenius K_p needs to be modified to minimize the percent difference. The adjust of $K_{p,o}$ is achieved by using by setting K_p in Eq. 28 and to the K_p at value at 625 C, which results in the values tabulated in Table 24.

Table 24 – Values to Calculate K_p at 625 C

$-Q/R$	$\ln(K_{p,0})$
-3.64E4	38.3

For the sake of completeness, the values in Table 23 result in a percent difference between the tabulated values in Table 4 and calculated values using Eq. 28 and Table 24 tabulated in Table 25.

Table 25 – Percent Difference Between K_p values from Table 4 and K_p values using Eq. 28 and Table 23

	600 C	625 C	650 C
K_p Table 4	1.738E-2	1.063E-1	1.251E-1
K_p Eq. 28, 600 – 650 C	3.35E-2	1.070E-1	3.21E-1
Percent Difference	63.4%	0.697%	87.8%

The next step in the Data Analysis is to apply the K_p value from Table 25 using Eq. 28 to predict the crack growth rates on the C(T) samples.

C. Finding Crack Growth Rates on C(T)

Figure 56 contains the crack size versus time data from the round robin samples.

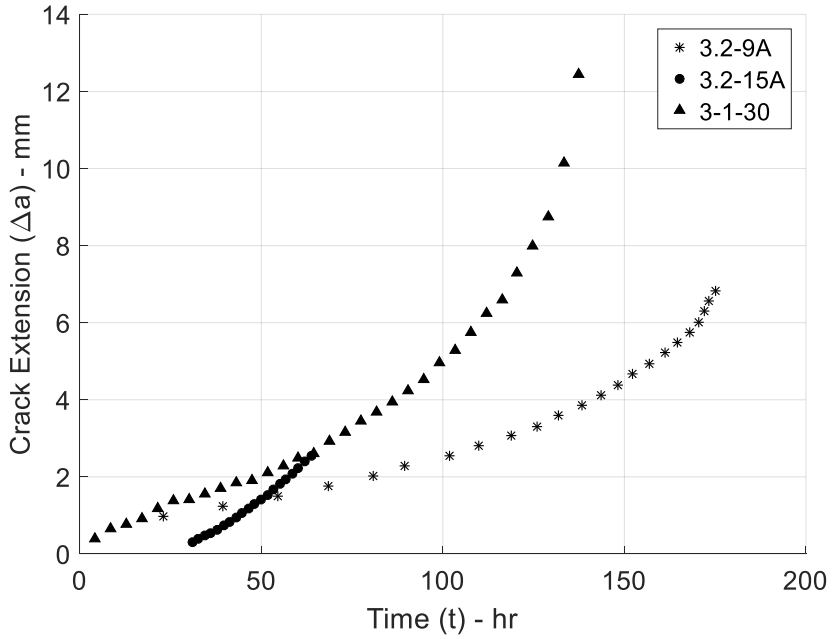

Figure 56 – R.R. Crack Extension vs Time

The crack growth rate at a given crack size is found using the seven-point incremental polynomial method. Matlab's polyfit function was used to find the polynomials for the method,

which finds a best-fit polynomial minimizing the sum of least-squares error. The polynomials are shown in the Appendix D Tables 37 through 39 for the following polynomial,

$$a = c_0 t^2 + c_1 t + c_2 \tag{38}$$

The crack growth data can be found by taking the derivative of the polynomial best fit, which becomes,

$$\frac{da}{\square t} = c_1 + 2c_1 t \tag{39}$$

and is tabulated in the Appendix D Tables 40 through 43. Figure 57 is the result of plugging in the time value at the midpoint to calculate the crack growth rate at the midpoint crack size value.

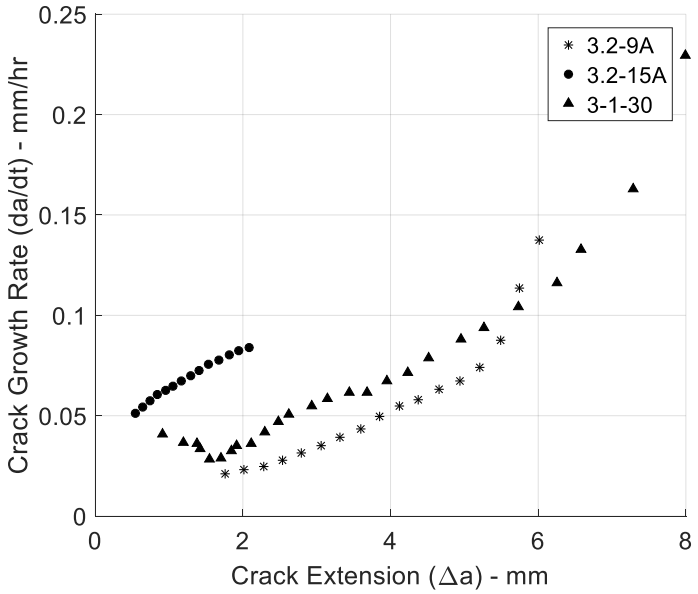

Figure 57 – Crack Growth Rates for C(T) Specimens

The means of applying the crack extension versus oxide thickness behavior to finding the crack growth rates requires a look at the ideal behavior as shown in Figure 58.

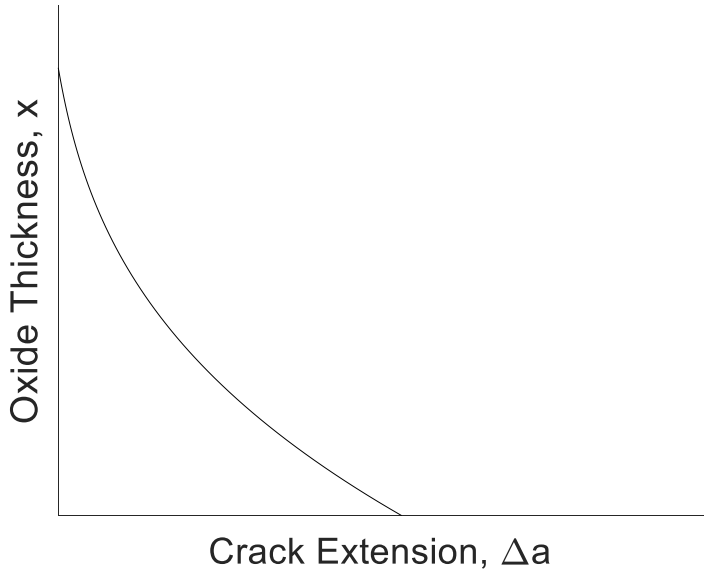

Figure 58 - ideal crack extension versus oxide thickness

Figure 58 shows that at the start or opening of the crack the oxide thickness is at the maximum value and then decreases when approaching the end. The crack extension versus oxide thickness behavior can be converted into the crack growth rate versus time by starting with the following,

$$\Delta a(x) = f(x) \tag{40}$$

where $f(x)$ is the function modeling the behavior. Next, taking the derivative leads to,

$$\frac{d(\Delta a)}{dx} = \frac{d(f(x))}{dx} \tag{41}$$

which when multiplied by the derivative of oxide thickness over time,

$$\frac{d(\Delta a)}{dt} = \frac{dx}{dt}\frac{d(f(x))}{dx} \tag{42}$$

However an issue arises with the behavior in Figure 58 and Eq. 42 is the negative value generated when finding the derivative, which does not match the crack growth rate behavior in Figure 57. The solution to this problem is the fact there is a difference in oxidation or exposure time and time the crack end point was at the crack extension value. The modeling of this time difference is,

$$t' = t_f - t \tag{43}$$

where t' is the time value at the crack extension value, t_f is the time value at the crack end point, and t is the oxidation or exposure time. The significant of Eq. 43 is being able to convert the oxidation or exposure time into the same time units of the C(T) data. Eq. 42 is converted into,

$$\frac{d(\Delta a)}{dt'} = \frac{dx}{dt'}\frac{d(f(x))}{dx} \tag{44}$$

where the derivative of the oxide thickness over time is modeled through Eq. 9 and 43. Staring with Eq. 9 and 43 the oxide thickness converted to time at the crack extension value is,

$$x = \sqrt{k_p\left(t_f - t'\right)} \tag{45}$$

and the derivative with respect to time is,

$$\frac{dx}{dt'} = -\frac{k_p}{2x} \tag{46}$$

which the negative sign value takes care of the negative slope of Figure 58. Combing Eq. 44 and 46 leads to the conversion of crack extension versus oxide thickness behavior to crack growth with,

$$\frac{d(\Delta a)}{dt'} = -\frac{k_p}{2x}\frac{d(f(x))}{dx} \tag{47}$$

or,

$$\frac{d(\Delta a)}{dt'} = -\frac{k_p}{2x\frac{dx}{d(f(x))}} \tag{48}$$

where the benefit of Eq. 48 is only the oxide thickness versus crack extension behavior is needed to find the crack growth rates. The actual crack extension versus oxide thickness behavior is shown in Figure 59.

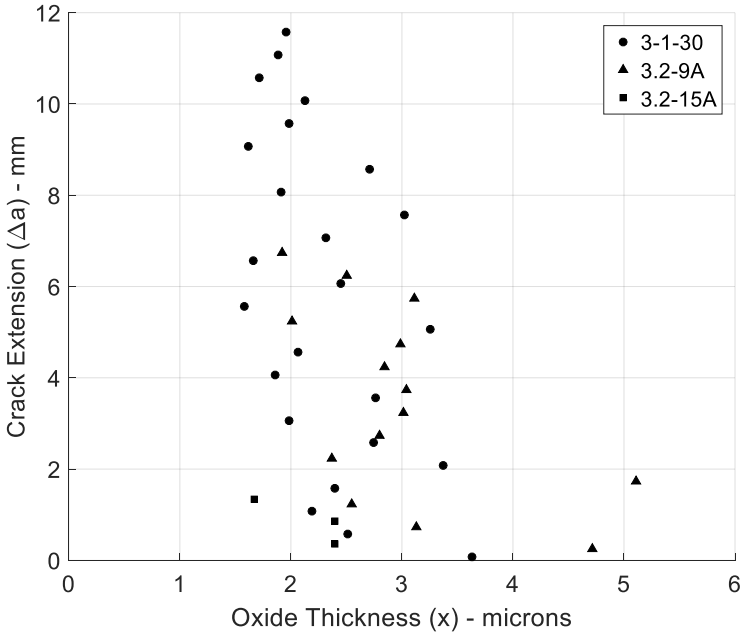

Figure 59 – Crack Extension vs Oxide Thickness

Figure 59 shows that there is a far amount of scatter in the oxide thickness values collected, which can be smoothed by using an averaging technique. The averaging technique can be shown by taking the original crack extension and oxide thickness data,

$$\Delta a = [\Delta a_i, \Delta a_{i+1}, \dots, \Delta a_{n-1}, \Delta a_n] \tag{49}$$

$$x = [x_i, x_{i+1}, \dots, x_{n-1}, x_n] \tag{50}$$

and apply the following,

$$x_{avg,j} = \frac{x_i + x_{i+1} + x_{i+2}}{3} \tag{51}$$

The corresponding crack extension value to $x_{avg,j}$ is,

$$\Delta a_{avg,j} = \Delta a_{i+1} \tag{52}$$

which leads to the crack extension and oxide thickness values to be,

$$\Delta a_{avg} = [\Delta a_{avg,j}, \Delta a_{avg,j+1}, \dots, \Delta a_{avg,m-1}, \Delta a_{avg,m}] \tag{53}$$

$$x_{avg} = [x_{avg,j}, x_{avg,j+1}, \dots, x_{av□,m-1}, x_{avg,m}] \tag{54}$$

where $j = i - 1$ and $m = n - 2$. Eq. 53 and 54 expressed in terms of the raw data in Eq. 49 and 50 are,

$$\Delta a_{avg} = [\Delta a_{i+1}, \Delta a_{i+2}, \dots, \Delta a_{n-2}, \Delta a_{n-1}] \tag{55}$$

$$x_{avg} = \left[\frac{x_i + x_{i+1} + x_{i+2}}{3}, \dots, \frac{x_{n-2} + x_{n-1} + x_n}{3}\right] \tag{56}$$

The downside to this method comes from the lose of two data points at the beginning and end, but the results applied to the crack extension versus oxide thickness behavior from Figure 59 as shown in Figure 60 show closer agreement to the ideal behavior seen in Figure 58.

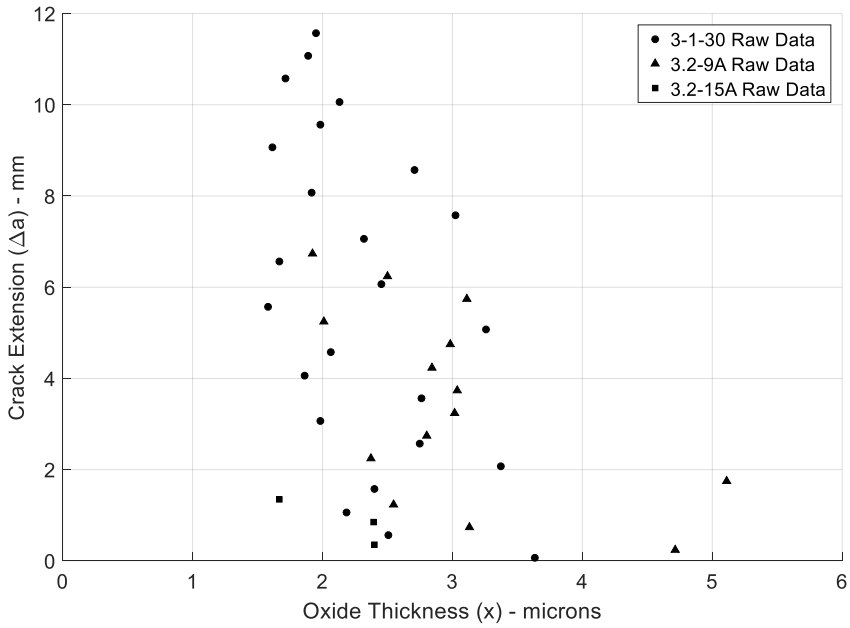

(a)

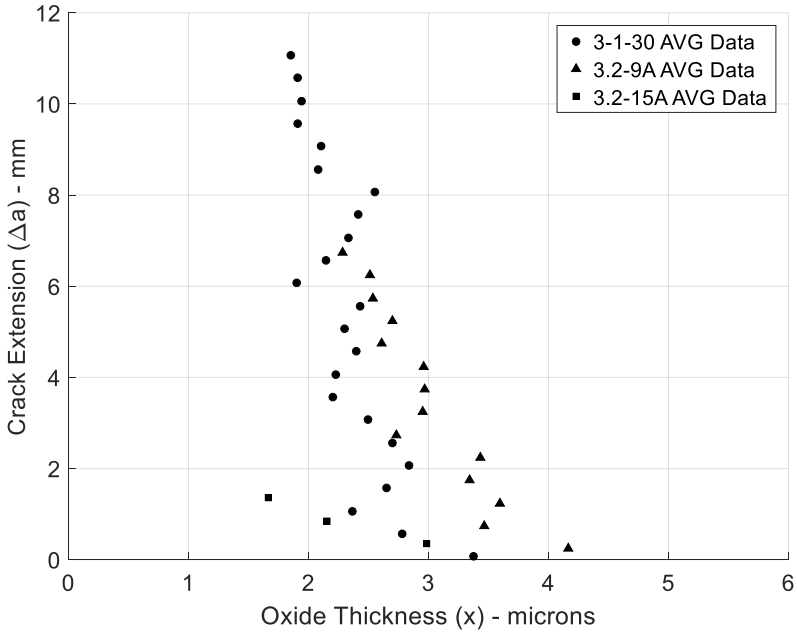

(b)

Figure 60 – Difference Between Raw Data (a) and AVG Data (b)

The crack extension versus oxide thickness behavior in Figure 60 does have one final difference from Figure 58 in that the oxide thickness does not approach zero at the end of crack extension. The oxide thickness does not approach zero on the C(T) specimens is most probably due to further oxidation between end of the R.R. and the application of Ni. Eq. 48's modeling of the crack growth rates can be found by the following second order polynomial,

$$x(\Delta a) = c_0 + c_1\left(1 - \frac{\Delta a}{\Delta a_f}\right) + c_2\left(1 - \frac{\Delta a}{\Delta a_f}\right)^2 \tag{57}$$

where Δa_f is the final crack extension value. The advantage of Eq. 57 is through generalizing the oxide versus crack extension behavior by dividing the crack extension, Δa, by the final crack extension value, Δa_f. Also, the reason Eq. 57 is a second order polynomial is that it is not derived from physics but experimental data. Eq. 57 applied to the averaged data in Figure 60 is seen in Figure 61 and constant tabulated in Table 26.

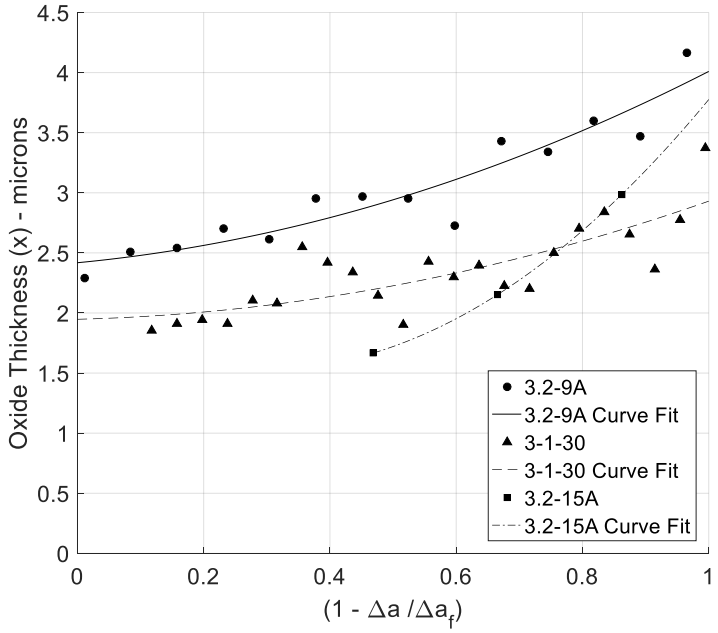

Figure 61 – C(T) Samples' Crack Extension vs Oxide Thickness Curve Fit

Table 26 - Curve Fit Values from Figure 61

C(T) Sample	c_0	c_1	c_2
3.2-9A	2.4181	0.5026	1.0892
3-1-30	1.9477	0.1314	0.8512
3.2-15A	1.9080	-2.6165	4.4832

Figure 61 for C(T) sample 3.2-15A shows the curve fit stopping at $\left(1-\frac{\Delta a}{\Delta a_f}\right)=0.4685$, which is due to not having data points between $0 \leq \left(1-\frac{\Delta a}{\Delta a_f}\right) < 0.4685$. When the 3.2-15A C(T) sample was converted into a SEM sample to measure the oxide thickness, the means of identifying the reference point for a_0 was lost. Instead of throwing the sample out, it was decided to build a model around if t_f was known. The logic is that if t_f is known then the oxide thickness at a_0 can be found with,

$$x_0 = \sqrt{K_p * t_f} \tag{58}$$

where x_0 is the oxide thickness at a_0. The addition benefit of Eq. 58 is that t_f can also be found at a_0 or $\left(1-\frac{\Delta a}{\Delta a_f}\right)=1$, by rearranging Eq. 60 into,

$$t_f = \frac{{x_0}^2}{K_p} \tag{59}$$

Using the values of Table 26 it is easy to find the value for x_0, since at a_0 Δa=0 and therefore x_0 = $c_0 + c_1 + c_2$ for the C(T). The relative error between the t_f from the C(T) data and t_f predicted from Eq. 57 and 59 using averaged or raw data is tabulated in Table 27.

Table 27 – Percent Difference between Measured t_f and Predicted t_f

C(T) Sample	3-1-30	3.2-9A	3.2-15A
C(T) t_f - hr	137.4	175.1	63.7
Eq. 59 using Eq. 57 and AVG Data - hr	80.2	150.3	133.2
Percent Difference	53.5%	15.25%	70.6%
Eq. 59 using Eq. 57 and Raw Data - hr	79.2	153.9	36.5
Percent Difference	53.8%	12.86%	54.4%

The decision to use the averaged or raw oxide thickness data depends only on 3-1-30 and 3.2-9A due to 3.2-15A being selected based on t_f and data points collected. Since there is not a large difference between using the raw and averaged oxide thickness data, the recommendation is to use the averaged oxide thickness data.

In order to show the validity of using the oxide thickness to predict the crack growth rates, the correlation between the crack growth rates predicted by the oxide and values measured by the C(T) data is found. The correlation between using Eq. 48 and the crack growth rates from Figure 57 is shown in Figure 62.

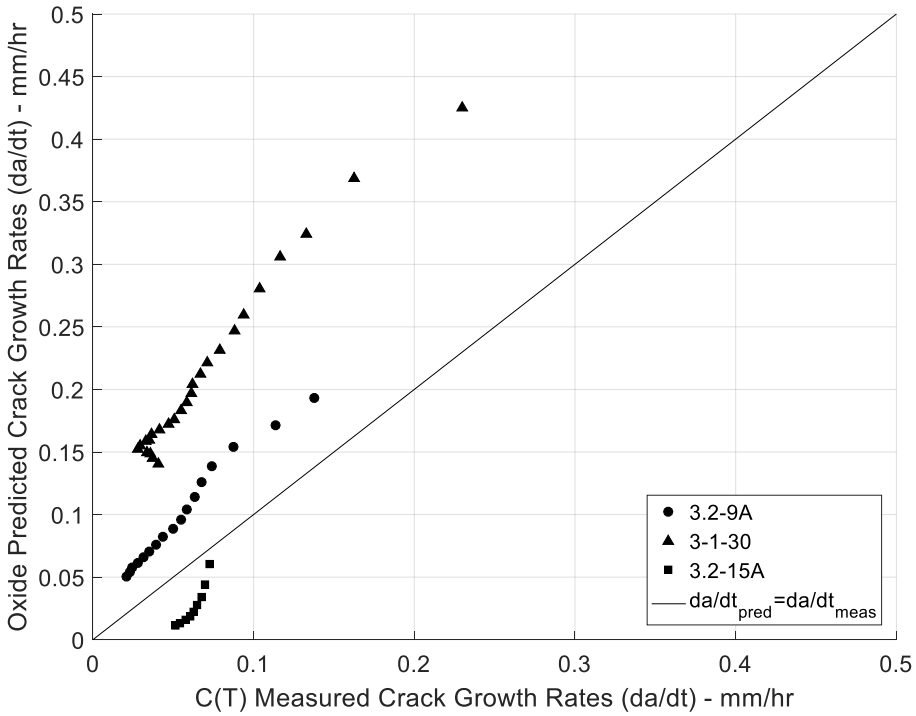

Figure 62 – Correlation Between Predicted Crack Growth Rates and Measured

The correlation fits used in Figure 62 are,

$$\frac{d(\Delta a)}{dt\prime}\Big]_{pred.} = c_0 \frac{d(\Delta a)}{dt\prime}\Big]_{meas.} + c_1 \tag{60}$$

$$\frac{d(\Delta a)}{dt\prime}\Big]_{pred.} = c_0 \frac{d(\Delta a)}{dt\prime}\Big]_{meas.} \tag{61}$$

where the correlation coefficients are tabulated in Table 28.

Table 28 - Correlation Coefficients From Figure 62

C(T) Sample	Eq. 60 c_0	Eq. 60 c_1	Eq. 61 c_0
3-1-30	1.549	0.1040	2.58
3.2-9A	1.303	0.0273	1.6715
3.2-15A	2.0751	-0.1016	0.4621

The correlation coefficients shown in Table 28 from Figure 62 show that the resultant predicted crack growth rates are within a factor of 1.303 to 2.0751 for c_0 from Eq. and 0.4621 and 2.58 for c_0 for Eq. 63 for 3-1-30, which shows the validity of the method. C(T) sample 3.2-15A exponential behavior is caused by the eventual extrapolation as the crack extension value goes

beyond $\left(1-\frac{\Delta a}{\Delta a_f}\right)=0.4685$, which again is due to only having oxide thickness data up to $\left(1-\frac{\Delta a}{\Delta a_f}\right)=0.4685$. The predicted versus actual crack growth values are left out of Figure 62 due to the predicted crack growth values become negative as Δa approaches Δa_f. The negative predicted values are not surprising due to trying to extrapolate values from a nonphysic but experimentally derived model. Therefore the recommendation is to make sure you have complete oxidation versus crack extension behavior for the sample. Figure 62 also shows a discontinuity between the last three crack growth values for C(T) samples 3.2-9A and 3-1-30, which is due to the sample entering into the third stage of creep crack growth. There are three possible reasons this discontinuity has arisen,

1. The model needs to be altered to account for the third stage of creep crack growth.
2. The resulting oxide thickness measurements during the third state of creep crack growth are hard to detect due to being near a_f or more measurements are needed as Δa increases.
3. The average smoothing technique masks the oxide thickness difference as Δa increases.

To better illustrate the discontinuities between the predicted and measured crack growth rates, the predicted and measured crack growth rates are plotted in Figure 63 versus crack extension.

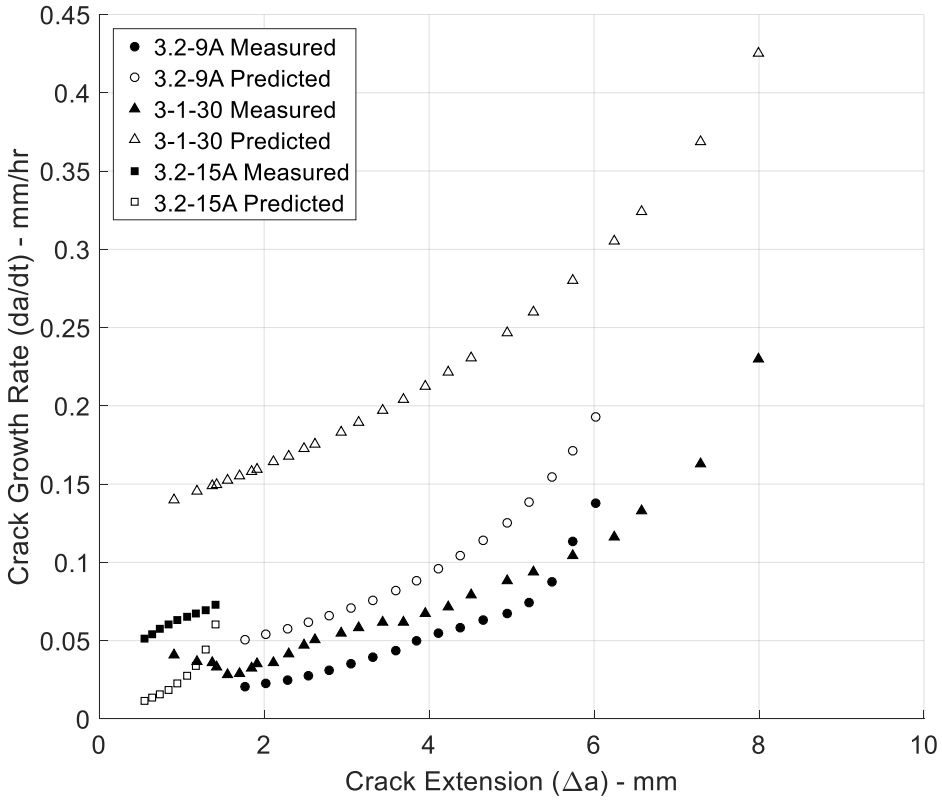

Figure 63 – Measured and Predicted Crack Growth Rates vs Crack Extension

Figure 63 illustrates better the assessment that the predicted crack growth rates from oxide thickness tend to over estimate the crack growth rates until the third stage of creep crack growth occurs

The correlations between the crack growth rates indicates that using the oxide thickness can successful predict creep crack growth rates in P91 steel components. Next will be to show the conclusions, area of future work, and how the techniques can be use on nonlaboratory specimens.

VI. Conclusions and Future Work

A. Conclusion

Through the use of a simple parabolic model of oxidation kinetics, the ability to predict the crack growth rates of P91 Steel components within a factor of 2.58 has been achieved. The methodology involved in finding these results are,

1. Measure the oxide thickness of test samples to find the parabolic rate constant.
2. Measure the oxide thickness versus crack extension response of the P91 steel component.
3. Apply the 2^{nd} degree polynomial, Eq. 57, to the oxide thickness versus crack extension response.
4. Use the parabolic rate constant and Eq. 57 to predict the crack growth rates using Eq. 47.

B. Future Work

Next, are the future works that are necessary to further validate this technique. The first major necessity of the techniques created through this research is to apply it to other materials. Another major caveat of applying this technique to a new material is if the oxidation kinetics does not match a parabolic model then Eq. 44 will need to be the starting point with the new oxide kinetics instead of Eq. 48. Another area of future work would be the application using Eq. 60 to predict the age of the crack. A plastic replica can be used to in real world applications to find the age of the crack, but finding an expectable value at which intervention is recommended based off crack age and component thickness is necessary. One final suggestion would be to use the type of oxides found on the P91 steel to predict the temperature the metal is at.

C. Improvements

Some improvements of the techniques would first be to change the Ni application portion of the sample preparation for SEM. Validation is necessary of course, but the Ni application stage

could be made unnecessary if the application of a conductive epoxy is made after the samples have had time to cool down after the furnace. The major advantage of skipping the Ni application set is the cost savings and time if and when this technique is applied in real life.

D. Application

The methodology of the application of this technique in nonlaboratory settings can be drawn from the results of this research. First the cracks in the P91 steel components can be found using plastic replicas since at the mouth of the cracks the oxide thickness, x_0, can predict the age of crack using Eq. 60. If the age of the crack based of oxide thickness is above expectable levels, the crack can be excavated from the component, an idealized exampled is shown in Figure 64.

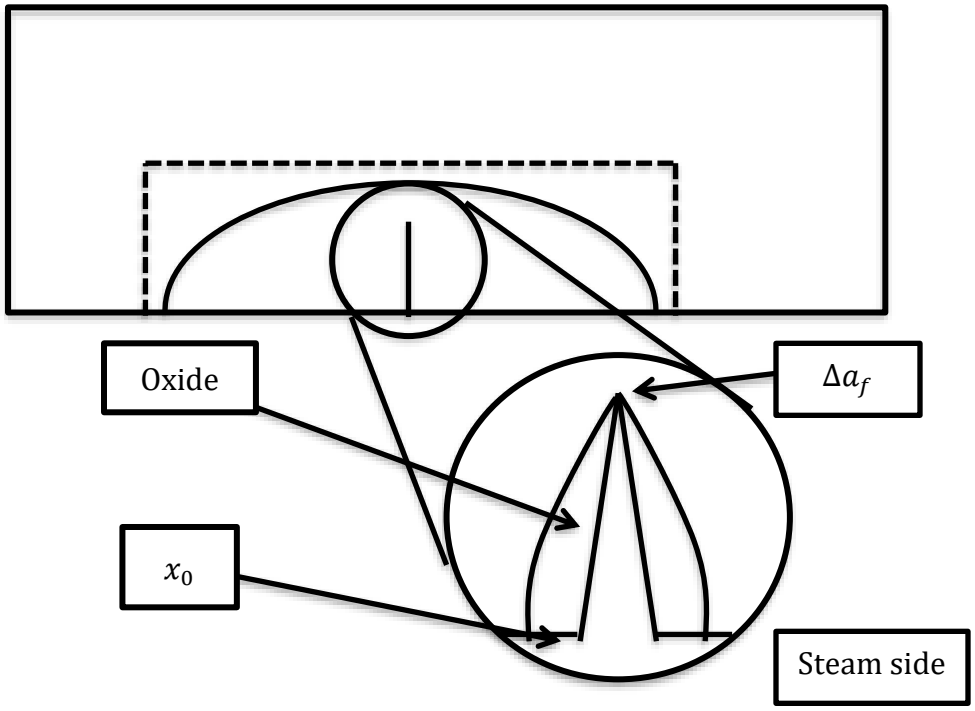

Figure 64 – Idealize Component with Known Crack

Next the crack surface will need to be exposed, which can be achieved by dipping the excavated crack region in liquid nitrogen and fracture the specimen to expose the fractured surface. Then the crack surface is coated with a hard epoxy (or Ni by electroplating or by physical vapor

decomposition followed by hard epoxy) that is either conductive or conductive filler material added to the epoxy. Once the epoxy has been applied, the sectioning of the specimen is necessary to expose the oxide thickness profile as shown in Figure 65.

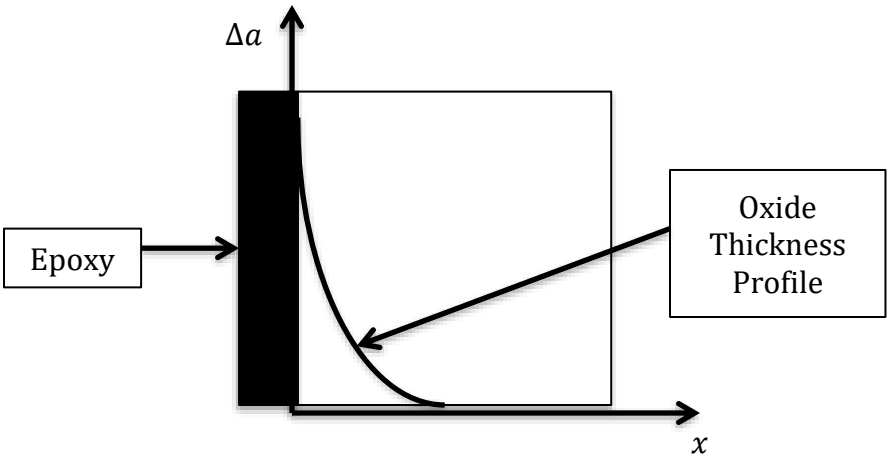

Figure 65 – Oxide thickness profile with Epoxy Coating

At this stage the oxide thickness profile versus crack extension can measured and used to predict the crack growth rates outlined in the data analysis Section C.

VII. References

1. A.Saxena, P.K. Liaw, and W.A. Logsdon, "Residual Life Prediction and Retirement for Cause Criteria for SSTG Upper Casings, Part II: Fracture Mechanics Analysis, Engineering Fracture Mechanics, vol. 25, 1986, pp. 289-303.

2. A. Saxena, Nonlinear Fracture Mechanics for Engineers, CRC Press, 199

3. A. Saxena editor, Comprehensive Structural Integrity, Volume 5-Creep, 2003

4. K.B. Yoon and A. Saxena, "An Interpretation of ΔJ for Cyclically Unsaturated Materials," International Journal of Fracture, July 1991.

5. K.B. Yoon, A. Saxena and P.K. Liaw, "Characterization of Creep-Fatigue Crack Growth Behavior Under Trapezoidal Waveshape Using C_t - Parameter," International Journal of Fracture, Vol. 59, 1993, pp. 95-114.

6. K.B. Yoon, A. Saxena and D.L. McDowell, "Effect of Cyclic Overload on the Crack Growth Behavior during Hold Period at Elevated Temperature", International Journal of Fracture, Vol. 59, 1993, pp. 199-211.

7. A. aSaxena, V. Kalyanasundaram and S.B. Narasimhachary, Prognostics for High Temperature Component Reliability", Invited Plenary Lecture, Thirteenth International Conference on Fracture, ICF13, Beijing, China, June 16-21, 2013.

8. ASTM Standard E 2714-13: Standard Test Method for Creep-Fatigue Testing, ASTM Book of Standards, ASTM International, W. Consohohocken, PA, 19428, 2013.

9. ASTM E2760-10: Standard Test Method for Creep-Fatigue Crack Growth Testing, ASTM Book of Standards, ASTM International, W. Consohohocken, PA, 19428, 2010.

10. L.W. Pinder, "Oxide Characterization for Service Failure Investigations", Corrosion Science, Vol. 21, No. 11, pp. 749 – 763, 1981.

11. N. Birks, G. H. Meier and F. S. Pettit, Introduction to High Temperature Oxidation, New York: Cambridge University Press, 2006.

12. Paul G. Shewmon, Diffusion in Solids, McGraw-Hill Book Company, Inc., 1963.

13. D. Young, High Temperature Oxidation and Corrosion of Metals, Oxford: Elsevier, 2008,.

14. T. Olszewski, "Oxidation Mechanisms of Materials for Heat Exchanging Components in $C0_2/H_2O$-containing Gases Relevant to Oxy-fuel Environments", Dissertation, RWTH Aachen University, 2012.

15. P. Mathiazhagan and A. S. Khanna, “High Temperature Oxidation Behavior of P91, P92 and E911 Alloy Steels in Dry and Wet Atmospheres,” High Temperature Material Process, Vol. 30, 2011, pp. 43 – 50.

16. ASTM Standard A335/A335M, 2011, “Standard Specification for Seamless Ferritic Alloy-Steel Pipe for High-Temperature Service,” ASTM International, West Conshokocken, PA, 2011, DOI: 10.1520/A0355_A0355M-11, www.astm.org.

17. Ashok Saxena, V. Kalyanasundaram and Stuart R. Holdsworth, “Final Report on Round-robin Conducted in Support of Standard Test Method for Creep-fatigue Testing”, EPRI Report 3002001719, Electric Power Research Institute, 3420 Hillview Ave., Palo Alto, CA, 94303, July 2013.

18. ASTM Standard E 3-11: Standard Guide for Preparation of Metallographic Specimens, ASTM Book of Standards, ASTM International, W. Consohohocken, PA, 19428, 2011.

19. J. Raja and T. V. Vorburger, Surface Finish Metrology Tutorial, National Institute of Standards and Testing, June 1990.

20. W. M. Haynes, David R. Lide and Thomas J. Bruno, CRC Handbook of Chemistry and Physics 97th Edition, CRC Press, Boca Raton, FL, 2017.

VIII. Appendix

A. Pretest and Posttest Weight of Oxidation Samples

Table 29 – Pretest and Posttest Weight at 600°C

Time	10	20	50	100	200	500	1000
Pretest 1 (g)	7.24564	7.28878	7.27957	7.27463	7.26885	7.42095	7.21839
Pretest 2 (g)	7.24566	7.28878	7.27959	7.27464	7.26888	7.42096	7.21842
Pretest 3 (g)	7.24565	7.2888	7.27959	7.27463	7.2689	7.42096	7.2184
Pretest 4 (g)	7.24565	7.28878	7.27958	7.27463	7.26888	7.42095	7.21842
Pretest Avg. (mg)	7245.650	7288.785	7279.583	7274.633	7268.878	7420.955	7218.408
Posttest1 (g)	7.24594	7.28935	7.28164	7.27877	7.27497	7.4289	7.22735
Posttest 2 (g)	7.24593	7.28934	7.28165	7.2788	7.27496	7.42891	7.22737
Posttest 3 (g)	7.24593	7.28935	7.28166	7.27879	7.27495	7.4289	7.22736
Posttest 4 (g)	7.24593	7.28936	7.28165	7.27879	7.27496	7.42890	7.22737
Posttest Avg. (mg)	7245.933	7289.350	7281.650	7278.788	7274.960	7428.903	7227.363

Table 30 – Pretest and Posttest Weight at 625°C

Time	10	20	50	100	200	500	1000
Pretest 1 (g)	7.24564	7.28878	7.27957	7.27463	7.26885	7.42095	7.21839
Pretest 2 (g)	7.24566	7.28878	7.27959	7.27464	7.26888	7.42096	7.21842
Pretest 3 (g)	7.24565	7.2888	7.27959	7.27463	7.2689	7.42096	7.2184
Pretest 4 (g)	7.24565	7.28878	7.27958	7.27463	7.26888	7.42095	7.21842
Pretest Avg. (mg)	7245.650	7288.785	7279.583	7274.633	7268.878	7420.955	7218.408
Posttest1 (g)	7.24594	7.28935	7.28164	7.27877	7.27497	7.4289	7.22735
Posttest 2 (g)	7.24593	7.28934	7.28165	7.2788	7.27496	7.42891	7.22737
Posttest 3 (g)	7.24593	7.28935	7.28166	7.27879	7.27495	7.4289	7.22736
Posttest 4 (g)	7.24593	7.28936	7.28165	7.27879	7.27496	7.42890	7.22737
Posttest Avg. (mg)	7245.933	7289.350	7281.650	7278.788	7274.960	7428.903	7227.363

Table 31 – Pretest and Posttest Weight at 650°C

Time	10	20	50	100	200	500
Pretest 1 (g)	7.39564	7.42999	7.25942	7.33011	7.40836	7.46305
Pretest 2 (g)	7.39566	7.42300	7.25944	7.33012	7.40837	7.46306
Pretest 3 (g)	7.39565	7.42999	7.25943	7.33012	7.40837	7.46306
Pretest 4 (g)	7.39565	7.42999	7.25943	7.3301	7.40836	7.46305
Pretest Avg. (mg)	7395.650	7428.243	7259.430	7330.113	7408.365	7463.055
Posttest 1 (g)	7.3969	7.43152	7.26655	7.34023	7.41956	7.48041
Posttest 2 (g)	7.39691	7.43152	7.26654	7.34024	7.41955	7.48042
Posttest 3 (g)	7.3969	7.43152	7.26655	7.34023	7.41956	7.48041
Posttest 4 (g)	7.3969	7.43152	7.26655	7.34022	7.41956	7.48042
Posttest Avg. (mg)	7396.903	7431.520	7266.548	7340.230	7419.558	7480.415

B. Parabolic Rate Constants in terms of mg^2*mm^-4*hr^-1

Table 32 – Parabolic Rate Constant (mg^2*mm^-4*hr-1) for 600°C

Time	10	20	50	100	200	500	1000
Diff Avg (mg)	2.82E-01	0.565	2.07	4.15	6.0825	7.9475	8.955
mg/mm^2	0.000403571	0.000807143	0.002953571	0.005935714	0.008689286	0.011353571	0.012792857
mg^2/mm^4	1.6287E-07	6.5148E-07	8.72358E-06	3.52327E-05	7.55037E-05	0.000128904	0.000163657
kp	1.6287E-08	3.2574E-08	1.74472E-07	3.52327E-07	3.77518E-07	2.57807E-07	1.63657E-07
Average kp	2.63399E-07						

Table 33 – Parabolic Rate Constant (mg^2*mm^-4*hr^-1) for 625°C

Time	50	100	500	1000
Diff Avg (mg)	8.4275	11.8975	24.0825	35.0600
mg/mm^2	0.012039286	0.016996429	0.034403571	0.050085714
mg^2/mm^4	0.000144944	0.000288879	0.001183606	0.002508579
Kp	2.89889E-06	2.88879E-06	2.36721E-06	2.50858E-06
Average kp	2.7183E-06			

Table 34 – Parabolic Rate Constant (mg^2*mm^-4*hr^-1) for 650°C

Time	10	20	50	100	200	500
Diff AVG (mg)	1.25E+00	3.2775	7.12E+00	1.01E+01	11.1925	17.36
mg/mm^2	0.001789286	0.004682143	0.010167857	0.014453571	0.015989286	0.0248
mg^2/mm^4	3.20154E-06	2.19225E-05	0.000103385	0.000208906	0.000255657	0.0006150 4
Kp	3.20154E-07	1.09612E-06	2.06771E-06	2.08906E-06	1.27829E-06	1.23008E-06
Average kp	1.3469E-06					

C. Different output results of MATLAB© edge Function

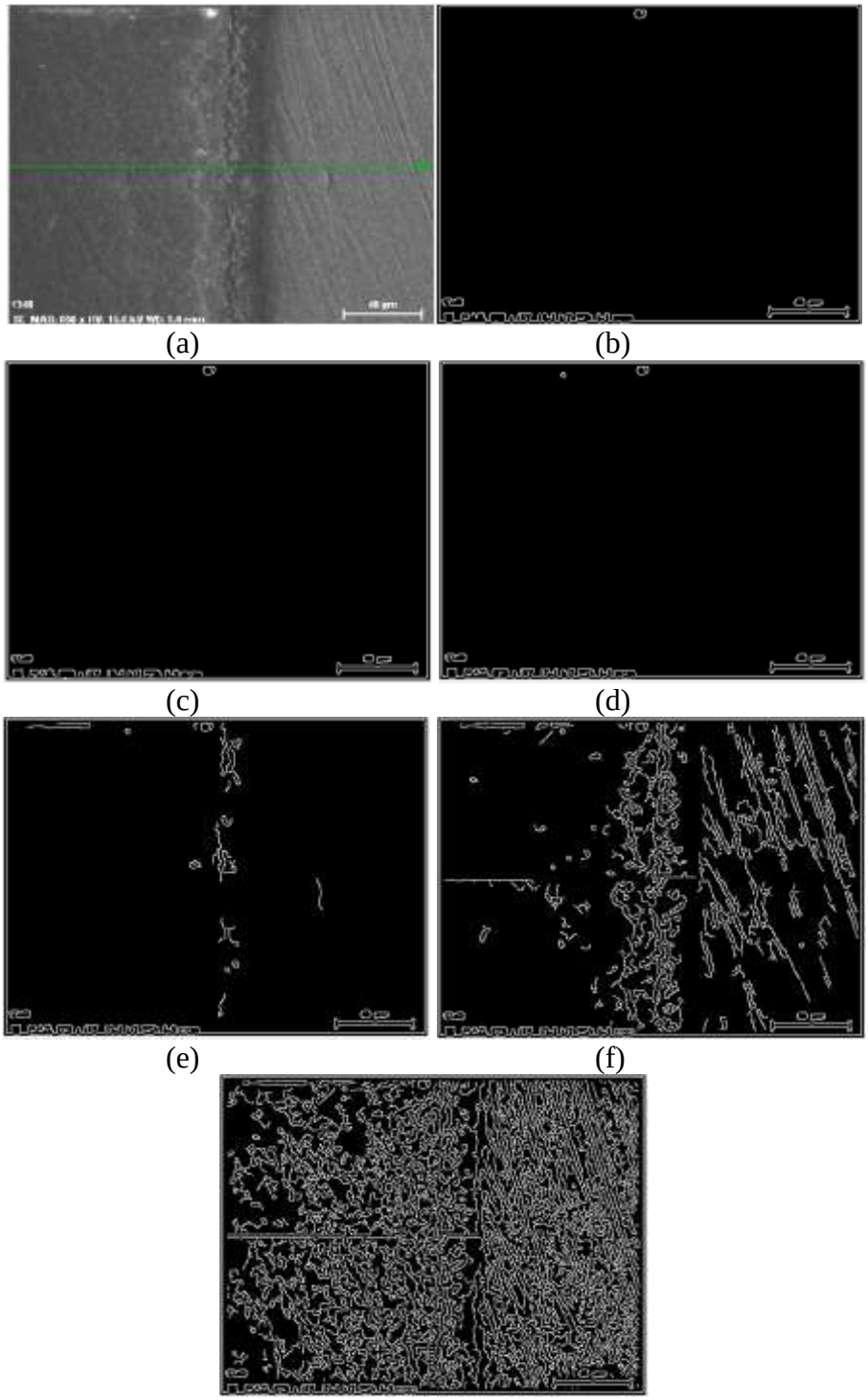

(a) (b) (c) (d) (e) (f) (g)

Figure 66 – Different Threshold Values for Canny Edge Method with MATLAB©
(a) Original SEM Picture (b) Threshold = 0.5 (c) Threshold = 0.4
(d) Threshold = 0.3 (e) Threshold = 0.2 (f) Threshold = 0.1 (g) Threshold = 0.05

D. Coefficients of Incremental Polynomial Method on C(T) Samples

Table 35 – Incremental Polynomial Method Results for Seven Points for 3.2-9A

Points	Midpoint	c_0	c_1	c_2
Points 1 thru 7	4	7.145006E-05	0.011043471	0.68261077
Points 2 thru 8	5	9.044903E-05	0.008382867	0.76931705
Points 3 thru 9	6	1.033412E-04	0.006210508	0.85719007
Points 4 thru 10	7	1.210847E-04	0.003212015	0.97858327
Points 5 thru 11	8	1.993915E-04	-0.012616345	1.76306290
Points 6 thru 12	9	2.764425E-04	-0.030600608	2.79879589
Points 7 thru 13	10	2.805735E-04	-0.031422634	2.83756195
Points 8 thru 14	11	3.633480E-04	-0.052438337	4.16333912
Points 9 thru 15	12	4.644522E-04	-0.078767897	5.86864625
Points 10 thru 16	13	5.410489E-04	-0.100705744	7.43321507
Points 11 thru 17	14	5.204065E-04	-0.096112138	7.20188762
Points 12 thru 18	15	4.227847E-04	-0.065556523	4.82060491
Points 13 thru 19	16	3.890278E-04	-0.054755228	3.95923992
Points 14 thru 20	17	7.928245E-04	-0.181332695	13.86383850
Points 15 thru 21	18	1.885888E-03	-0.532976616	42.11329494
Points 16 thru 22	19	3.557308E-03	-1.082219451	87.19797485
Points 17 thru 23	20	5.275101E-03	-1.660017604	135.75733105

Table 36 – Incremental Polynomial Method Results for Seven Points for 3.2-15A

Points	Midpoint	c_0	c_1	c_2
Points 1 thru 7	4	8.830088E-04	-0.012857143	-0.13761904
Points 2 thru 8	5	1.083693E-03	-0.027995392	0.146428570
Points 3 thru 9	6	1.003419E-03	-0.022050691	0.03714286
Points 4 thru 10	7	6.823250E-04	0.003940093	-0.48666667
Points 5 thru 11	8	6.020514E-04	0.010990783	-0.64071428
Points 6 thru 12	9	6.020514E-04	0.010990782	-0.64071426
Points 7 thru 13	10	6.823250E-04	0.003940092	-0.48666667
Points 8 thru 14	11	8.027352E-04	-0.007741934	-0.20428575
Points 9 thru 15	12	8.830088E-04	-0.015622119	-0.01142858
Points 10 thru 16	13	8.027353E-04	-0.007465438	-0.21809522
Points 11 thru 17	14	6.823250E-04	0.004907834	-0.53500000
Points 12 thru 18	15	6.020514E-04	0.013894009	-0.78571429
Points 13 thru 19	16	6.020514E-04	0.01389401	-0.78571431
Points 14 thru 20	17	4.816412E-04	0.027788018	-1.18571426

Table 37 – Incremental Polynomial Method Results for Seven Points for 3-1-30

Points	Midpoint	c_0	c_1	c_2
Points 1 thru 7	4	-2.48857E-04	0.049301152	0.20380641
Points 2 thru 8	5	-3.38600E-04	0.051476803	0.19908477
Points 3 thru 9	6	-6.35517E-04	0.068934511	-0.03543684
Points 4 thru 10	7	-4.25692E-04	0.05908904	0.06700755
Points 5 thru 11	8	-4.43989E-05	0.031338733	0.54961385
Points 6 thru 12	9	2.57457E-04	0.009133441	0.94538237
Points 7 thru 13	10	1.99893E-04	0.015513275	0.78313747
Points 8 thru 14	11	3.99326E-04	-0.002789696	1.1946669
Points 9 thru 15	12	3.45895E-04	0.000530683	1.16348347
Points 10 thru 16	13	6.06303E-04	-0.026266577	1.84055292
Points 11 thru 17	14	4.28691E-04	-0.004687365	1.19373468
Points 12 thru 18	15	6.73617E-04	-0.036150039	2.19313562
Points 13 thru 19	16	5.47647E-04	-0.020608951	1.72227308
Points 14 thru 20	17	2.98137E-04	0.014826589	0.47453702
Points 15 thru 21	18	-9.45539E-07	0.061690569	-1.34610887
Points 16 thru 22	19	2.16739E-04	0.026197611	0.09080732
Points 17 thru 23	20	6.06598E-04	-0.037252906	2.6536298
Points 18 thru 24	21	7.69107E-04	-0.067792033	4.07632593
Points 19 thru 25	22	9.55805E-04	-0.102167012	5.65078299
Points 20 thru 26	23	1.18857E-03	-0.147060734	7.80570871
Points 21 thru 27	24	5.92550E-04	-0.02877799	1.96440636
Points 22 thru 28	25	9.67196E-04	-0.104145304	5.73018013
Points 23 thru 29	26	1.77820E-03	-0.281944244	15.44122954
Points 24 thru 30	27	2.06055E-03	-0.346287256	19.09505246
Points 25 thru 31	28	4.16470E-03	-0.841453715	48.13781444
Points 26 thru 32	29	9.06670E-03	-2.034517135	120.5246076

Table 38 – Crack Growth Rates for 3.2-9A

Points	Midpoint	c_0	c_1
Points 1 through 7	4	1.429001E-04	0.011043471
Points 2 through 8	5	1.808981E-04	0.008382867
Points 3 through 9	6	2.066823E-04	0.006210508
Points 4 through 10	7	2.421693E-04	0.003212015
Points 5 through 11	8	3.987831E-04	-0.012616345
Points 6 through 12	9	5.528851E-04	-0.030600608
Points 7 through 13	10	5.611470E-04	-0.031422634
Points 8 through 14	11	7.266960E-04	-0.052438337
Points 9 through 15	12	9.289043E-04	-0.078767897
Points 10 through 16	13	1.082098E-03	-0.100705744
Points 11 through 17	14	1.040813E-03	-0.096112138
Points 12 through 18	15	8.455694E-04	-0.065556523
Points 13 through 19	16	7.780556E-04	-0.054755228
Points 14 through 20	17	1.585649E-03	-0.181332695
Points 15 through 21	18	3.771776E-03	-0.532976616
Points 16 through 22	19	7.114615E-03	-1.082219451
Points 17 through 23	20	1.055020E-02	-1.660017604

Table 39 – Crack Growth Rates for 3.2-15A

Points	Midpoint	c_0	c_1
Points 1 through 7	4	1.766018E-03	-0.012857143
Points 2 through 8	5	2.167385E-03	-0.027995392
Points 3 through 9	6	2.006838E-03	-0.022050691
Points 4 through 10	7	1.364650E-03	0.003940093
Points 5 through 11	8	1.204103E-03	0.010990783
Points 6 through 12	9	1.204103E-03	0.010990782
Points 7 through 13	10	1.364650E-03	0.003940092
Points 8 through 14	11	1.605470E-03	-0.007741934
Points 9 through 15	12	1.766018E-03	-0.015622119
Points 10 through 16	13	1.605471E-03	-0.007465438
Points 11 through 17	14	1.364650E-03	0.004907834
Points 12 through 18	15	1.204103E-03	0.013894009
Points 13 through 19	16	1.204103E-03	0.01389401
Points 14 through 20	17	9.632823E-04	0.027788018

Table 40 – Crack Growth Rates for 3-1-30

Points	Midpoint	c_0	c_1
Points 1 through 7	4	-4.97714E-04	0.049301152
Points 2 through 8	5	-6.77199E-04	0.051476803
Points 3 through 9	6	-1.27103E-03	0.068934511
Points 4 through 10	7	-8.51383E-04	0.05908904
Points 5 through 11	8	-8.87978E-05	0.031338733
Points 6 through 12	9	5.14915E-04	0.009133441
Points 7 through 13	10	3.99786E-04	0.015513275
Points 8 through 14	11	7.98651E-04	-0.002789696
Points 9 through 15	12	6.91789E-04	0.000530683
Points 10 through 16	13	1.21261E-03	-0.026266577
Points 11 through 17	14	8.57383E-04	-0.004687365
Points 12 through 18	15	1.34723E-03	-0.036150039
Points 13 through 19	16	1.09529E-03	-0.020608951
Points 14 through 20	17	5.96273E-04	0.014826589
Points 15 through 21	18	-1.89108E-06	0.061690569
Points 16 through 22	19	4.33479E-04	0.026197611
Points 17 through 23	20	1.21320E-03	-0.037252906
Points 18 through 24	21	1.53821E-03	-0.067792033
Points 19 through 25	22	1.91161E-03	-0.102167012
Points 20 through 26	23	2.37714E-03	-0.147060734
Points 21 through 27	24	1.18510E-03	-0.02877799
Points 22 through 28	25	1.93439E-03	-0.104145304
Points 23 through 29	26	3.55639E-03	-0.281944244
Points 24 through 30	27	4.12110E-03	-0.346287256
Points 25 through 31	28	8.32941E-03	-0.841453715
Points 26 through 32	29	1.81334E-02	-2.034517135

Table 41 – Crack Growth Rate Values for 3.2-9A

Midpoint	Crack Size - mm	Crack Growth Rate – mm/hr
4	1.7631	2.0841E-02
5	2.0171	2.2994E-02
6	2.2787	2.4736E-02
7	2.5403	2.7874E-02
8	2.7943	3.1263E-02
9	3.0585	3.5135E-02
10	3.3176	3.9236E-02
11	3.5944	4.3441E-02
12	3.8535	4.9848E-02
13	4.1177	5.4731E-02
14	4.3793	5.8094E-02
15	4.6587	6.3116E-02
16	4.9432	6.7286E-02
17	5.2124	7.4277E-02
18	5.4944	8.7656E-02
19	5.7484	1.1345E-01
20	6.0151	1.3773E-01

Table 42 – Crack Growth Rate Values for 3.2-15A

Midpoint	Crack Size - mm	Crack Growth Rate – mm/hr
4	0.55	5.101382E-02
5	0.64	5.412442E-02
6	0.74	5.744240E-02
7	0.84	6.034562E-02
8	0.95	6.283410E-02
9	1.06	6.490783E-02
10	1.17	6.739631E-02
11	1.29	6.967742E-02
12	1.41	7.258065E-02
13	1.54	7.548387E-02
14	1.67	7.776498E-02
15	1.81	8.025346E-02
16	1.95	8.232719E-02
17	2.09	8.419355E-02

Table 43 – Crack Growth Rate Values for 3-1-30

Midpoint	Crack Size - mm	Crack Growth Rate – mm/hr
4	1.010614429	4.07294E-02
5	1.291303343	3.68982E-02
6	1.473264721	3.60995E-02
7	1.521953304	3.34293E-02
8	1.653113036	2.82801E-02
9	1.807045371	2.90864E-02
10	1.950199537	3.27263E-02
11	2.014758923	3.50353E-02
12	2.214540384	3.62731E-02
13	2.393542647	4.16057E-02
14	2.581902119	4.69938E-02
15	2.717291653	5.08588E-02
16	3.031324309	5.48446E-02
17	3.250772927	5.84705E-02
18	3.537016801	6.15440E-02
19	3.782911962	6.16586E-02
20	4.05257111	6.72168E-02
21	4.332238252	7.12882E-02
22	4.616258306	7.89049E-02
23	5.049290172	8.83421E-02
24	5.369598518	9.36824E-02
25	5.836682932	1.04071E-01
26	6.348537516	1.16174E-01
27	6.679565422	1.32791E-01
28	7.385188569	1.62703E-01
29	8.093081728	2.29639E-01